

# Heterogeneous graph attention network improves cancer multiomics integration

Sina Tabakhi<sup>1, 2</sup>, Charlotte Vandermeulen<sup>3</sup>, Ian Sudbery<sup>3</sup>, and Haiping Lu<sup>1, 2\*</sup>

<sup>1</sup>School of Computer Science, The University of Sheffield, Sheffield, UK

<sup>2</sup>Centre for Machine Intelligence, The University of Sheffield, Sheffield, UK

<sup>3</sup>School of Biosciences, The University of Sheffield, Sheffield, UK

\*corresponding author: Haiping Lu (h.lu@sheffield.ac.uk)

## ABSTRACT

The increase in high-dimensional multiomics data demands advanced integration models to capture the complexity of human diseases. Graph-based deep learning integration models, despite their promise, struggle with small patient cohorts and high-dimensional features, often applying independent feature selection without modeling relationships among omics. Furthermore, conventional graph-based omics models focus on homogeneous graphs, lacking multiple types of nodes and edges to capture diverse structures. We introduce a **Heterogeneous Graph AT**tention network for **omics** integration (HeteroGATomics) to improve cancer diagnosis. HeteroGATomics performs joint feature selection through a multi-agent system, creating dedicated networks of feature and patient similarity for each omic modality. These networks are then combined into one heterogeneous graph for learning holistic omic-specific representations and integrating predictions across modalities. Experiments on three cancer multiomics datasets demonstrate HeteroGATomics' superior performance in cancer diagnosis. Moreover, HeteroGATomics enhances interpretability by identifying important biomarkers contributing to the diagnosis outcomes.

## Introduction

Recent advancements in sequencing technologies have significantly accelerated the generation of multimodal biological data, collectively known as multiomics. This progress enables personalized medicine by constructing comprehensive patient profiles across multiple omic modalities<sup>1,2</sup>. While each omic modality contains valuable information, their collective integration enables new insights into the fundamental aspects of human disease biology, particularly in cancer research<sup>3,4</sup>. Research initiatives developing integrative multiomics models<sup>2,5,6</sup> leverage the unique and complementary characteristics of each modality to construct multimodal models that are more accurate and interpretable than unimodal models, thereby enhancing biological predictions and facilitating biomarker discovery<sup>3,6,7</sup>. There are three main modality fusion strategies<sup>2,8</sup>. *Early* fusion concatenates features from different input modalities<sup>9</sup>, combining all modalities at the raw feature level. *Joint* or *intermediate* fusion processes each modality independently before integrating their low-level representations<sup>5,10</sup>, enabling more effective interactions among modalities at a lower dimensionality. *Late* fusion develops separate models for each modality and merges their predictions<sup>11</sup>, leveraging unimodal strengths and addressing multiomics heterogeneity.

More recently, deep learning on graphs (or networks), referred to as graph neural networks (GNNs)<sup>12</sup>, has been increasingly utilized for multiomics integration<sup>4,7,13,14</sup>. GNNs offer more accurate models with improved decision-making power by effectively capturing both the intra- and inter-omic structures within the data. Modeling each omic modality as a graph, where biological entities are nodes and their interactions are edges, facilitates a deeper understanding of entity interactions<sup>7</sup>. Graph attention networks (GATs) are a class of GNNs that extend this capability by using an attention mechanism to learn varying importance for different interactions<sup>15</sup>. This approach enhances the model's ability to focus on the most relevant biological relationships within multiomics datasets<sup>16</sup>.

GNNs in multiomics analysis, while promising, still face two key challenges. The first challenge is learning from high-dimensional data, where each omic suffers from having a large number of features compared to a small patient cohort<sup>1,17</sup>. This issue hinders the ability of GNNs to learn meaningful representations, reducing performance in biomedical applications<sup>5</sup>. Most current studies apply feature selection strategies independently to each omic modality<sup>4,8</sup>, without accounting for relationships among them, which can compromise interpretability and model performance. A few studies have explored joint feature selection across all omics<sup>18,19</sup>, yet these often involve either a single-iteration greedy process or creating fully connected graphs rather than sparse graphs in feature space, leading to reduced predictive capability or high computational demands. Therefore, there is a clear gap in the development of better methods that effectively account for intra- and inter-omic relationships in multiomics.

The second challenge is the limited expressive power of conventional GNNs developed for homogeneous graphs. In these models<sup>4,6,13</sup>, the learning process incorporates only patient or feature similarity networks with a single type of node and edge.

Representing multiple input modalities as a homogeneous graph loses crucial structural information inherent in the data, fails to account for the diverse nature of the data, and limits the model's ability to capture complex biological interactions. In contrast, heterogeneous graphs offer a solution to these limitations by modeling multiple types of nodes and edges to capture the diversity of the data. While some methods have extended learning to heterogeneous graphs<sup>16,20,21</sup>, they often rely on pre-existing knowledge graphs to represent semantic relationships between different entities, such as genes, patients, and diseases. However, such pre-existing knowledge graphs may not always be available, and creating them often requires domain knowledge or expertise and can be costly<sup>22</sup>.

Here, we present HeteroGATomics, a novel framework employing heterogeneous GAT for integrating multiomics data for cancer diagnosis. HeteroGATomics operates in two distinct stages: joint feature selection and heterogeneous graph learning. Unlike previous feature selection methods, HeteroGATomics implements a multi-agent system (MAS) for a joint feature selection on sparse graphs, constructed across the feature spaces of all omics. This approach creates a *feature similarity network* for each modality, representing one view of the input data. The proposed joint feature selection strategy not only achieves competitive performance but also captures structural features arising from MAS. Moreover, for each omic modality, a *patient similarity network* is built, forming the second data view. We propose a dual-view approach to automatically construct modality-specific heterogeneous graphs by connecting feature and patient similarity networks, followed by representation learning with GAT encoders to generate predictions. This heterogeneous graph construction improves the expressive power of GATs by capturing diverse structural information. Leveraging late fusion for final decision-making in HeteroGATomics integrates predictions from all modalities in a supervised manner for multiomics integration<sup>4</sup>.

We conduct comprehensive experiments to evaluate HeteroGATomics' diagnosis performance on three cancer multiomics datasets. The results show that HeteroGATomics consistently outperforms baseline methods, highlighting the benefits of integrating diverse omics data. Additionally, we show the necessity of each module of HeteroGATomics via a series of ablation studies. We further explore HeteroGATomics' interpretability through a biomarker identification process, revealing its ability to identify cancer-related biomarkers. By pinpointing interacting biomarker networks and highlighting key cancer-related functions, it also identifies potential therapeutic targets.

## Results

### HeteroGATomics architecture

HeteroGATomics performs supervised multiomics integration with two main modules: an MAS for dimensionality reduction of preprocessed omics and a GAT architecture for heterogeneous graph representation learning, as shown in Fig. 1.

HeteroGATomics first represents each preprocessed omic as a sparse feature similarity network, where each node corresponds to an individual feature and each edge indicates the correlation between a pair of features (Fig. 1a and Supplementary Fig. S6). Then, it uses the MAS algorithm to jointly select features from all omic modalities, leveraging both intra- and cross-modality interactions at the feature level (see [Methods](#)) to utilize complementary information in multiomics datasets.

After joint feature selection, HeteroGATomics creates a patient similarity network for each omic, where nodes represent patients and edges represent correlations between their features. Next, it constructs a heterogeneous graph for each omic modality by connecting the patient and feature similarity networks, connecting feature nodes to all patient nodes (Fig. 1b). This helps capture patient-level and feature-level relationships in a unified representation, providing a comprehensive view of the dataset. Then, a heterogeneous GAT model encodes the structures inherent in each input heterogeneous graph and learns meaningful node representations (Fig. 1c). Afterward, a single-layer fully connected neural network takes the learned node representations as input to predict cancer. Finally, a late fusion strategy consolidates predictions across modalities by aggregating the generated predictions and feeding them into a view correlation discovery network (VCDN)<sup>4</sup> for final prediction. The model architecture and implementation details are provided in [Methods](#) and Supplementary Section S4.3, respectively.

To the best of our knowledge, HeteroGATomics is the first method to explore cross-modality interactions at both the feature level, using the MAS algorithm, and the label level, employing a late fusion strategy. Moreover, the joint feature selection algorithm in HeteroGATomics not only reduces feature dimensionality but also provides more structural information for the heterogeneous graph, benefiting downstream tasks.

### Datasets

We evaluate HeteroGATomics performance across three multiomics datasets derived from The Cancer Genome Atlas (TCGA) cohort, for two downstream tasks, including bladder urothelial carcinoma (BLCA) grade classification, brain lower grade glioma (LGG) grade classification, and renal cell carcinoma (RCC) subtype classification. We download all datasets from the TCGA cohort via the UCSC Xena platform<sup>23</sup>, which includes DNA methylation (DNA), gene expression RNAseq (mRNA), and miRNA mature strand expression RNAseq (miRNA). Our analysis retains only patients with available information in all omic modalities. Each omic modality in every dataset undergoes individual preprocessing to address missing values, normalize features, and eliminate low-variance features (see [Methods](#)). Table 1 summarizes the dataset characteristics for each phase.

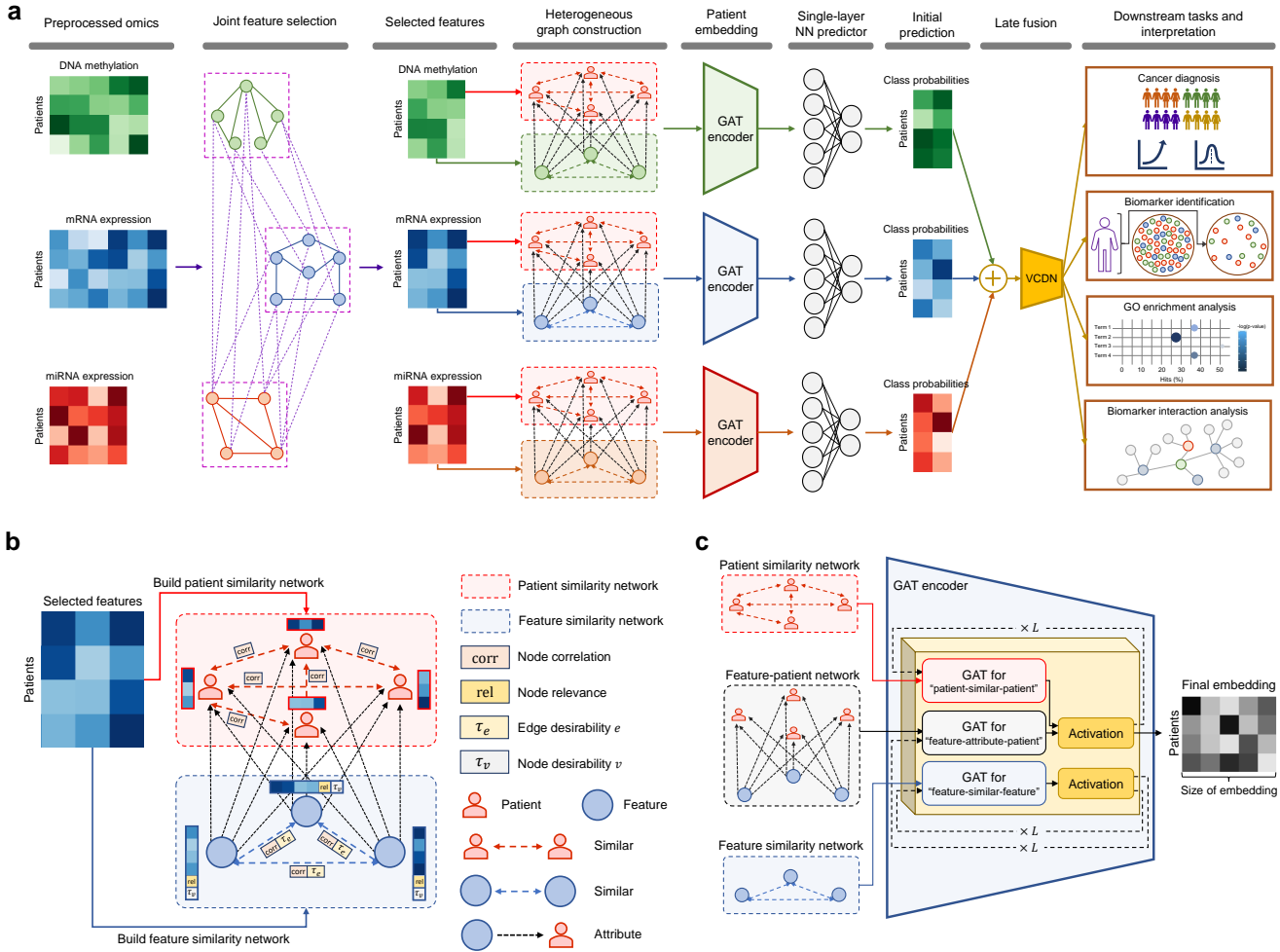


**Fig. 1. HeteroGATomics architecture.** **a**, HeteroGATomics integrates joint feature selection and heterogeneous graph learning in six steps. (1) HeteroGATomics represents the preprocessed omics as feature similarity networks, where each network represents a specific omic with nodes corresponding to features and edges denoting their correlations. All omic modalities are interconnected at the raw feature level to capture cross-modality interactions. (2) An MAS performs joint feature selection on these networks to select informative features, considering both intra- and cross-modality interactions. (3) HeteroGATomics builds a patient similarity network for each omic and combines it with the feature similarity network to construct a heterogeneous graph. (4) GAT encoders learn the representations of each individual heterogeneous graph. (5) A single-layer neural network predicts patient labels from the learned representations. (6) A late fusion combines predicted labels from all modalities and feeds them into a VCDN network to perform downstream tasks. **b**, The heterogeneous graph construction combines feature and patient similarity networks through feature-patient relations. **c**, Multiple stacked GAT layers (denoted by  $L$ ) encodes the heterogeneous graph into hidden representations for each node type. Each layer uses three GATs to learn the three relations within the graph, updating node representations by aggregating relation-specific information.

BLCA is the most common type of bladder cancer, more prevalent in men than women, and can be grouped into low-grade and high-grade cases<sup>24</sup>. LGG is a type of primary brain tumor that includes grades II and III for classification purposes<sup>25</sup>. RCC is the most prevalent type of kidney cancer in adults, which has kidney chromophobe (KICH), kidney clear cell carcinoma (KIRC), and kidney papillary cell carcinoma (KIRP) as the most frequent histological subtypes<sup>26</sup>.

### Evaluation strategies and metrics

We evaluate the classification performance on the three datasets using stratified 10-fold cross-validation. This approach ensures robust performance evaluation by splitting each dataset into training and test sets while maintaining a balanced class representation. In each fold, nine sets are used for training, further split into training and validation sets at a 9:1 ratio, while

**Table 1. A summary of multiomics data characteristics at each preprocessing stage.**

| Dataset | Categories                     | Number of patients | Number of original features |        |       | Number of features after missing value removal |        |       | Number of features after variance filtering |       |       |
|---------|--------------------------------|--------------------|-----------------------------|--------|-------|--|--------|-------|---|-------|-------|
|         |                                |                    | DNA                         | mRNA   | miRNA | DNA  | mRNA   | miRNA | DNA   | mRNA  | miRNA |
| BLCA    | High-grade: 397, Low-grade: 21 | 418                | 485,577                     | 20,530 | 2,210 | 382,545  | 20,530 | 249   | 7,999                                       | 2,373 | 249   |
| LGG     | Grade II: 254, Grade III: 268  | 522                | 485,577                     | 20,530 | 2,157 | 370,278  | 20,530 | 287   | 8,277                                       | 1,166 | 287   |
| RCC     | KICH: 65, KIRC: 201, KIRP: 294 | 560                | 485,577                     | 20,530 | 1,847 | 377,787  | 20,530 | 238   | 4,107                                       | 2,456 | 238   |

the remaining set is used for testing. This process is repeated ten times, ensuring each set is used for testing exactly once. We report the mean and the standard deviation of the evaluation metrics calculated on the test sets across experiments. For the hyperparameter configuration of HeteroGATomics, we report the mean of the evaluation metrics calculated on the validation sets. To ensure a fair comparison across different methods, we maintain identical splits for all evaluations. Details of the optimal hyperparameter configuration are provided in Supplementary Section S5.

To evaluate model performance for binary classification tasks, we use six metrics, including area under the receiver operating characteristic curve (AUROC), accuracy, negative predictive values (NPVs), positive predictive values (PPVs), sensitivity, and specificity. For multi-class classification, we use six metrics, including accuracy, macro-averaged F1 score (Macro F1), micro-averaged F1 score (Micro F1), weighted-averaged F1 score (Weighted F1), precision, and recall.

### Classification performance comparison

We compare the classification performance of HeteroGATomics with that of eight multiomics integration methods. We adopt early fusion using five classifiers— $k$ -nearest neighbors (KNN)<sup>27</sup>, multilayer perceptron (MLP)<sup>27</sup>, random forest (RF)<sup>28</sup>, Ridge regression (Ridge)<sup>29</sup>, gradient tree boosting (XGBoost)<sup>30</sup>—concatenating 100 features from each modality selected by mutual information (MI)<sup>27</sup> (see Supplementary Section S2). We also utilize joint feature selection techniques by minimal-redundancy–maximal-relevance multi-view (mRMR-mv)<sup>18</sup> and the multi-agent architecture for multi-omics (MAgentOmics)<sup>19</sup>, each selecting 300 features collectively from all modalities based on their respective strategies. Moreover, we select multi-omics graph convolutional networks (MOGONET)<sup>4</sup>, a supervised late fusion method, incorporating 100 selected features per modality using MI for a fair comparison. Table 2 presents the detailed classification comparisons for the BLCA, LGG, and RCC datasets.

From Table 2, we observe that HeteroGATomics outperforms baseline multiomics integration methods for the binary classification task on BLCA and LGG in terms of AUROC, accuracy, NPV, PPV, sensitivity, and specificity, except for specificity in BLCA, and NPV and sensitivity in LGG. HeteroGATomics still achieves the second-best in NPV for LGG. Furthermore, Table 2 demonstrates HeteroGATomics’ superiority for the multi-class classification task on RCC, excelling in all the evaluated metrics.

The outstanding performance of HeteroGATomics indicates that the combined power of its multi-agent feature selection module (that is, HeteroGATomics<sub>MAS</sub>) and GAT module (that is, HeteroGATomics<sub>GAT</sub>) trained on generated heterogeneous graphs significantly enhances the capabilities of a deep learning model for multiomics integration. We show a comprehensive performance study of the standalone feature selection module of HeteroGATomics in Supplementary Section S2.

### Ablation studies

We conduct ablation studies to examine the impact of individual modules within HeteroGATomics and assess its effectiveness in integrating different modalities. First, we highlight the crucial role of HeteroGATomics<sub>GAT</sub> in augmenting the predictive capabilities of HeteroGATomics architecture for classification tasks, beyond what its HeteroGATomics<sub>MAS</sub> can achieve. Figure 2 compares the whole HeteroGATomics pipeline against HeteroGATomics<sub>MAS</sub> on the BLCA, LGG, and RCC datasets. We show HeteroGATomics<sub>MAS</sub>’s performance using KNN, MLP, RF, Ridge, and XGBoost classifiers. Figure 2 shows the addition of the heterogeneous GAT module (HeteroGATomics<sub>GAT</sub>) significantly boosts HeteroGATomics’ performance with an improvement of 16.7%, 5.7%, and 0.4% in AUROC on BLCA, LGG, and RCC, respectively. These results highlight the value of the heterogeneous GAT module in HeteroGATomics to enhance its multiomics integration capabilities.

We next demonstrate the effectiveness of heterogeneous graphs and their impact on GAT performance. We conduct several modifications: removing the feature similarity network to simulate a homogeneous graph scenario (denoted as Homogeneous), removing correlation and edge desirability derived from the MAS module as edge attributes (denoted as Hetero<sub>Feature</sub>), and excluding relevance and node desirability derived from the same module as node attributes (denoted as Hetero<sub>Edge</sub>). We refer to the full HeteroGATomics architecture, incorporating both node and edge attributes, as Hetero<sub>Feature+Edge</sub>. The results of this comparative study on LGG in Fig. 3 show that HeteroGATomics, when leveraging heterogeneous graphs, outperforms its homogeneous graph counterpart, achieving improvements of 2.3%, 1.6%, 2.3%, and 2.4% in accuracy, AUROC, sensitivity, and specificity, respectively. Furthermore, the enhancement in HeteroGATomics’ performance comes not only from the feature similarity network but also from the contributions of each individual network element, including feature and edge attributes.

**Table 2. Classification performance comparison with mean  $\pm$  standard deviation over 10-fold cross-validation.**

| Dataset | Metric      | KNN <sup>27</sup>                   | MLP <sup>27</sup>                   | RF <sup>28</sup>                    | Ridge <sup>29</sup>                 | XGBoost <sup>30</sup>               | mRMR-mv <sup>18</sup> | MAgentOmics <sup>19</sup>           | MOGONET <sup>4</sup>                | HeteroGATomics                      |
|---------|-------------|-------------------------------------|-------------------------------------|-------------------------------------|-------------------------------------|-------------------------------------|-----------------------|-------------------------------------|-------------------------------------|-------------------------------------|
| BLCA    | AUROC       | 0.779 $\pm$ 0.191                   | 0.744 $\pm$ 0.194                   | 0.684 $\pm$ 0.149                   | 0.720 $\pm$ 0.129                   | 0.760 $\pm$ 0.175                   | 0.683 $\pm$ 0.146     | 0.572 $\pm$ 0.114                   | 0.884 $\pm$ 0.160                   | <b>0.961 <math>\pm</math> 0.065</b> |
|         | Accuracy    | 0.955 $\pm$ 0.027                   | <u>0.962 <math>\pm</math> 0.026</u> | 0.955 $\pm$ 0.022                   | <u>0.962 <math>\pm</math> 0.016</u> | <b>0.964 <math>\pm</math> 0.016</b> | 0.952 $\pm$ 0.018     | 0.952 $\pm$ 0.015                   | 0.948 $\pm$ 0.023                   | <b>0.964 <math>\pm</math> 0.027</b> |
|         | NPV         | <u>0.978 <math>\pm</math> 0.020</u> | 0.973 $\pm$ 0.023                   | 0.968 $\pm$ 0.016                   | 0.971 $\pm$ 0.018                   | 0.976 $\pm$ 0.019                   | 0.968 $\pm$ 0.015     | 0.957 $\pm$ 0.014                   | 0.961 $\pm$ 0.019                   | <b>0.983 <math>\pm</math> 0.016</b> |
|         | PPV         | 0.517 $\pm$ 0.329                   | 0.583 $\pm$ 0.417                   | 0.600 $\pm$ 0.436                   | <u>0.650 <math>\pm</math> 0.391</u> | <u>0.650 <math>\pm</math> 0.369</u> | 0.500 $\pm$ 0.387     | 0.250 $\pm$ 0.403                   | 0.292 $\pm$ 0.407                   | <b>0.673 <math>\pm</math> 0.360</b> |
|         | Sensitivity | <u>0.583 <math>\pm</math> 0.382</u> | 0.500 $\pm$ 0.387                   | 0.383 $\pm$ 0.299                   | <u>0.450 <math>\pm</math> 0.269</u> | 0.533 $\pm$ 0.356                   | 0.383 $\pm$ 0.299     | 0.150 $\pm$ 0.229                   | 0.250 $\pm$ 0.335                   | <b>0.667 <math>\pm</math> 0.316</b> |
|         | Specificity | 0.975 $\pm$ 0.020                   | 0.987 $\pm$ 0.017                   | 0.985 $\pm$ 0.020                   | <u>0.990 <math>\pm</math> 0.017</u> | 0.987 $\pm$ 0.013                   | 0.982 $\pm$ 0.020     | <b>0.995 <math>\pm</math> 0.010</b> | 0.985 $\pm$ 0.023                   | 0.980 $\pm$ 0.027                   |
| LGG     | AUROC       | 0.670 $\pm$ 0.052                   | 0.697 $\pm$ 0.043                   | 0.704 $\pm$ 0.055                   | 0.650 $\pm$ 0.049                   | 0.679 $\pm$ 0.078                   | 0.687 $\pm$ 0.051     | 0.685 $\pm$ 0.035                   | 0.716 $\pm$ 0.050                   | <b>0.766 <math>\pm</math> 0.046</b> |
|         | Accuracy    | 0.667 $\pm$ 0.053                   | 0.695 $\pm$ 0.044                   | <u>0.703 <math>\pm</math> 0.056</u> | 0.649 $\pm$ 0.049                   | 0.678 $\pm$ 0.078                   | 0.686 $\pm$ 0.053     | 0.684 $\pm$ 0.035                   | 0.674 $\pm$ 0.060                   | <b>0.711 <math>\pm</math> 0.042</b> |
|         | NPV         | 0.630 $\pm$ 0.056                   | 0.673 $\pm$ 0.050                   | <b>0.686 <math>\pm</math> 0.071</b> | 0.634 $\pm$ 0.048                   | 0.657 $\pm$ 0.076                   | 0.670 $\pm$ 0.069     | 0.666 $\pm$ 0.042                   | 0.674 $\pm$ 0.073                   | <u>0.675 <math>\pm</math> 0.054</u> |
|         | PPV         | <u>0.737 <math>\pm</math> 0.066</u> | 0.726 $\pm$ 0.043                   | 0.735 $\pm$ 0.058                   | 0.671 $\pm$ 0.059                   | 0.715 $\pm$ 0.108                   | 0.716 $\pm$ 0.047     | 0.711 $\pm$ 0.048                   | 0.681 $\pm$ 0.057                   | <b>0.783 <math>\pm</math> 0.067</b> |
|         | Sensitivity | 0.552 $\pm$ 0.116                   | 0.653 $\pm$ 0.084                   | <u>0.664 <math>\pm</math> 0.118</u> | 0.631 $\pm$ 0.073                   | 0.638 $\pm$ 0.107                   | 0.645 $\pm$ 0.126     | 0.653 $\pm$ 0.078                   | <b>0.689 <math>\pm</math> 0.102</b> | 0.619 $\pm$ 0.120                   |
|         | Specificity | <u>0.788 <math>\pm</math> 0.077</u> | 0.740 $\pm$ 0.050                   | 0.745 $\pm$ 0.083                   | 0.670 $\pm$ 0.078                   | 0.721 $\pm$ 0.114                   | 0.729 $\pm$ 0.072     | 0.718 $\pm$ 0.068                   | 0.657 $\pm$ 0.079                   | <b>0.808 <math>\pm</math> 0.088</b> |
| RCC     | Accuracy    | 0.946 $\pm$ 0.028                   | 0.954 $\pm$ 0.024                   | 0.950 $\pm$ 0.026                   | 0.954 $\pm$ 0.024                   | <u>0.955 <math>\pm</math> 0.022</u> | 0.954 $\pm$ 0.021     | 0.950 $\pm$ 0.024                   | 0.952 $\pm$ 0.025                   | <b>0.961 <math>\pm</math> 0.019</b> |
|         | Macro F1    | 0.944 $\pm$ 0.025                   | 0.953 $\pm$ 0.024                   | 0.950 $\pm$ 0.020                   | 0.949 $\pm$ 0.025                   | <u>0.955 <math>\pm</math> 0.019</u> | 0.953 $\pm$ 0.018     | 0.948 $\pm$ 0.021                   | 0.953 $\pm$ 0.022                   | <b>0.957 <math>\pm</math> 0.026</b> |
|         | Micro F1    | 0.946 $\pm$ 0.028                   | 0.954 $\pm$ 0.024                   | 0.950 $\pm$ 0.026                   | 0.954 $\pm$ 0.024                   | <u>0.955 <math>\pm</math> 0.022</u> | 0.954 $\pm$ 0.021     | 0.950 $\pm$ 0.024                   | 0.952 $\pm$ 0.025                   | <b>0.961 <math>\pm</math> 0.019</b> |
|         | Weighted F1 | 0.947 $\pm$ 0.028                   | 0.953 $\pm$ 0.025                   | 0.950 $\pm$ 0.026                   | 0.954 $\pm$ 0.024                   | <u>0.955 <math>\pm</math> 0.022</u> | 0.954 $\pm$ 0.022     | 0.950 $\pm$ 0.024                   | 0.952 $\pm$ 0.026                   | <b>0.961 <math>\pm</math> 0.019</b> |
|         | Precision   | 0.949 $\pm$ 0.027                   | 0.958 $\pm$ 0.021                   | 0.953 $\pm$ 0.025                   | 0.956 $\pm$ 0.024                   | <u>0.959 <math>\pm</math> 0.020</u> | 0.956 $\pm$ 0.021     | 0.953 $\pm$ 0.023                   | 0.956 $\pm$ 0.023                   | <b>0.964 <math>\pm</math> 0.019</b> |
|         | Recall      | 0.946 $\pm$ 0.028                   | 0.954 $\pm$ 0.024                   | 0.950 $\pm$ 0.026                   | 0.953 $\pm$ 0.024                   | <u>0.955 <math>\pm</math> 0.021</u> | 0.954 $\pm$ 0.021     | 0.950 $\pm$ 0.023                   | 0.952 $\pm$ 0.025                   | <b>0.961 <math>\pm</math> 0.019</b> |

The best performance for each metric in each dataset is denoted in **bold**, with the second-best results underlined.

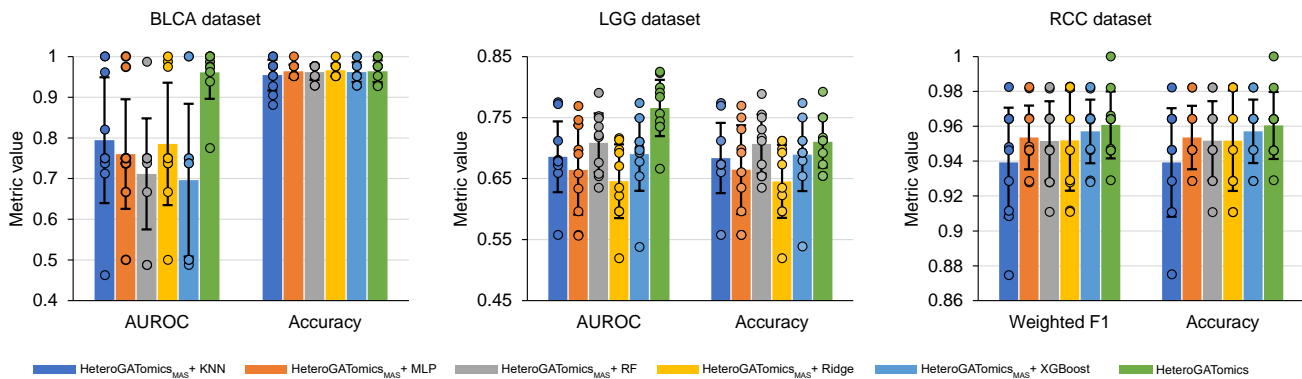


**Fig. 2. Performance comparison of HeteroGATomics with its feature selection module across five classifiers (mean and standard deviation over 10-fold cross-validation).** The vertical bars show the mean, the black lines represent error bars indicating plus/minus one standard deviation, and each dot is a model’s performance on each fold. HeteroGATomics<sub>MAS</sub> + [classifier] denotes the results of the feature selection module within HeteroGATomics for a classifier, while HeteroGATomics represents the results derived from the entire HeteroGATomics architecture.

To evaluate the impact of different omic modalities on HeteroGATomics’ performance and to determine the benefit of integrating multiple omics, we train HeteroGATomics using seven modality combinations: individual modalities without the VCDN module (DNA, mRNA, and miRNA), combinations of two modalities (DNA+mRNA, DNA+miRNA, mRNA+miRNA), and all three modalities together (DNA+mRNA+miRNA). The performance of these configurations is assessed on LGG in AUROC, accuracy, sensitivity, and specificity. The results in Fig. 4 show that integrating additional omic modalities with HeteroGATomics enhances its performance across various evaluation metrics, except for specificity. In the context of single-modality learning, mRNA contributes significantly to the performance, particularly in AUROC and accuracy. Notably, integrating all three modalities outperforms single or dual-modality combinations, further highlighting the benefits of multiomics integration via HeteroGATomics. We also report an execution time analysis for training HeteroGATomics with all modality combinations in Supplementary Section S6.

### Analysis of identified biomarkers for cancer diagnosis

To understand the decision-making process within HeteroGATomics, we utilize a biomarker importance extraction technique (see Supplementary Section S4.2) to identify and analyze the key biomarkers that significantly influence the classification results. Table 3 presents the 30 most important biomarkers identified by HeteroGATomics on BLCA and LGG. RCC is excluded

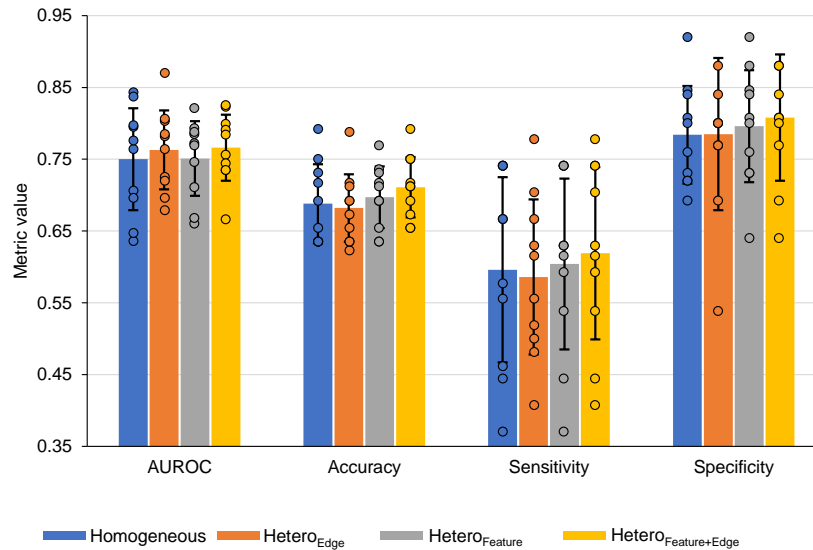


**Fig. 3. Comparison of HeteroGATomics performance with and without heterogeneous graphs on the LGG dataset (mean and standard deviation over 10-fold cross-validation).** The vertical bars show the mean, the black lines represent error bars indicating plus/minus one standard deviation, and each dot is a model's performance on each fold. Homogeneous refers to HeteroGATomics without the feature similarity network, Hetero<sub>Feature</sub> removes edge attributes (correlation, edge desirability), Hetero<sub>Edge</sub> excludes node attributes (relevance, node desirability), and Hetero<sub>Feature+Edge</sub> represents the full HeteroGATomics setup.

from further biomarker identification, serving only as a proof-of-concept for multi-class classification tasks<sup>4</sup>.

Top ranking biomarkers for LGG consist of 16 DNA methylation features, 13 mRNAs, and 1 miRNA. BLCA consists of 14 mRNA features, 11 DNA methylation features, and 5 miRNAs. Gene ontology (GO) enrichment analysis on the top 30 DNA and mRNA biomarkers highlights terms related to synaptic and signal transduction for LGG (GO:0097060,  $p=0.009$  and GO:0007165,  $p=0.012$ , see Supplementary Fig. S3a). Belonging to those categories is PTPRA, a protein tyrosine phosphatases with known roles in tumorigenesis<sup>31</sup>. CHRND and KCNC2, ion channels genes, also belong to both categories. Numerous ion channels are dysregulated in glioma and significantly impact prognosis<sup>32</sup>. Xu *et al.* have previously identified KCNC2 as downregulated in malignant gliomas<sup>33</sup>, while CHRND has been identified as a biomarker for treatment and prognosis of head and neck cell carcinomas<sup>34</sup>.

GO terms related to the top BLCA biomarkers include several developmental processes (e.g. Regionalization,  $p=0.008$ , see Supplementary Fig. S3b). This emphasises top biomarkers that are Transcription Factors (TFs), essential regulators of gene expression: YBX2, HOXB2 and 3, FOXH1, FOXA3, DMRTA2, TEX15 and MAGEA10. These have diverse functions: DNA repair, cell differentiation and migration, cell cycle and organogenesis to cite a few, all relevant in the context of cancer. Among them, TFs of the Fox superfamily FOXH1 and FOXA3 are identified as mRNA biomarkers. FOX family proteins have been shown to be involved in bladder development and cancer progression, for instance FOXA1 expression has been correlated to poor survival<sup>35</sup>. For DNA methylation features, HOXB2 has recently been shown to be upregulated in some subtypes of BLCA and to act as a tumor promoter<sup>36</sup>. All of the following genes identified by HeteroGATomics have been previously flagged as potential biomarkers for BLCA: YBX2<sup>37</sup>, DMRTA2<sup>38</sup>, TEX15<sup>39</sup> and MAGEA10<sup>40</sup>.

Notably, the top 5 biomarkers of BLCA are all miRNAs, small RNAs known for regulating gene expression post-transcriptionally by binding target mRNAs and preventing their translation via degradation or translational silencing. As such they play a central role in cell maintenance and in tumorigenesis. Numerous studies have pointed out the importance of miRNAs in bladder cancer and their potential use in cancer diagnosis and prognosis<sup>41,42</sup>. All 5 miRNAs have been studied in the context of other cancers, for example pancreas and liver<sup>43</sup> or breast<sup>44</sup>. Three of our five (hsa-mir-1-3p, hsa-mir-708-5p and hsa-mir-16-2-3p), have been previously linked to bladder cancer<sup>45-47</sup>. Zhang *et al.* demonstrated that hsa-mir-1-3p is downregulated in bladder cancer tissues and is able to inhibit cancer proliferation and tumorigenesis *in vivo*<sup>48</sup>. HeteroGATomics is able to not only identify known miRNAs related to bladder cancer but also identify new potential miRNAs, hsa-mir-1976 and hsa-mir-24-3p, involved in oncogenesis.

We further investigate the interaction network of the top biomarkers, including protein-binding partners of protein coding biomarkers and targets of miRNAs biomarkers (Fig. 5 and Supplementary Figs. S4 and S5). Interestingly, the BLCA miRNA

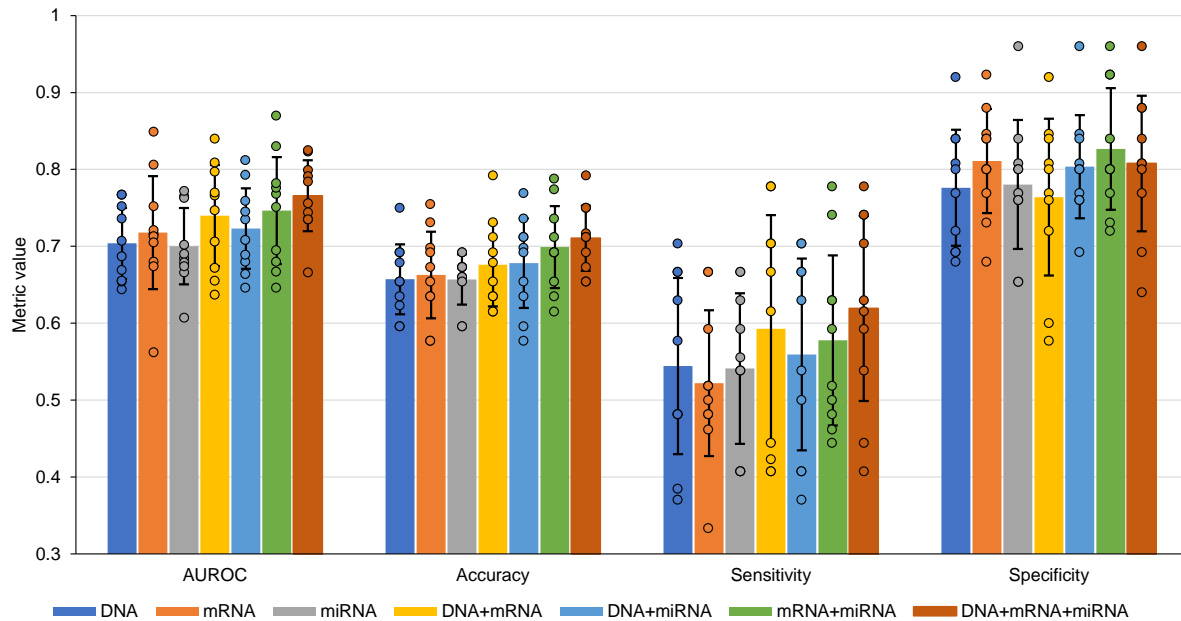


**Fig. 4. Performance comparison of HeteroGATomics across different combinations of modalities on the LGG dataset (mean and standard deviation over 10-fold cross-validation).** The vertical bars show the mean, the black lines represent error bars indicating plus/minus one standard deviation, and each dot is a model's performance on each fold. DNA, mRNA, and miRNA refer to the single-modality classification performance on DNA methylation, gene expression RNase, and miRNA mature strand expression RNaseq, respectively. Two-modality combinations refer to DNA+mRNA, DNA+miRNA, and mRNA+miRNA, while DNA+mRNA+miRNA refers to the classification performance across three modalities. In each case, 300 features are selected and divided equally among the modalities.

biomarker hsa-mir-708-5p targets four of the protein-coding biomarkers, while hsa-mir-1-3p targets three. This includes partners such as HOXB2 and YBX2, suggesting a possible regulation between them (Fig. 5a). Examining the protein-protein interactions of the LGG biomarkers shows that RAD9A has numerous protein partners and many are known genes related to cancer (Fig. 5b and Supplementary Fig. S5). RAD9A itself is involved in DNA repair, interacts with several components of the DNA damage response pathways that is targeted for glioblastoma treatment<sup>49</sup>. For instance, RAD9A interacts with ATR to mediate DNA repair and several ATR inhibitor drugs have been developed for treating Glioblastoma<sup>49,50</sup>. RAD9A also interacts with HDAC1, a mediator of chromatin compaction, known to be frequently overexpressed in LGG and also targeted for therapy<sup>51</sup>. Interestingly, another biomarker, MIDEAS, also interacts with HDAC1, as well as with HDAC2 (Fig. 5b), forming part of the mitotic deacetylase (MiDAC) complex, which is important for neuronal development<sup>52</sup>.

The homeobox TF CUX1 is another important component of LGG. Like MIDEAS, CUX1 is also a target of the miRNA biomarker hsa-mir-363-3p (Fig. 5b). Moreover, CUX1 has been previously identified as widely expressed in glioma. CUX1 seems to promote tumorigenesis via the Wnt/b-Catenin pathway<sup>53</sup>. Another biomarker, RBMS3, is an RNA binding protein that regulates crucial cellular processes such as transcription, cell apoptosis or cell cycle progression. Its expression correlates with good or poor prognosis depending on cancer type<sup>54</sup>. Ruan *et al.* recently discovered that RBMS3 downregulation leads to increased proliferation of glioblastoma cells by interacting with circHECTD1. Subsequently increasing VE-cadherin levels and promoting vasculogenic mimicry, which has a deleterious effect on anti-vascular therapy<sup>55</sup>. HeteroGATomics also highlights deletion of BRINP1, also known as DBC1 for deleted in bladder cancer 1. Silencing of, or deletions on, chromosome 9 are known in the context of bladder cancer and include silencing of BRINP1. BRINP1 has been shown to suppress cell cycle progression and to be a candidate tumor suppressor<sup>56</sup>.

## Discussion

The development of cancer involves multiple biological layers. The availability of diverse biological data, multiomics, offers detailed insights into various cancer mechanisms. However, integrating multiple heterogeneous omic datasets for cancer diagnosis and biomarker identification remains a significant challenge, especially in small patient cohorts with high-dimensional

**Table 3. Top 30 ranked biomarkers identified by HeteroGATomics in the BLCA and LGG datasets.**

| BLCA |              |                     |       | LGG  |              |                                       |       |
|------|--------------|---------------------|-------|------|--------------|---------------------------------------|-------|
| Rank | Biomarker ID | Biomarker name      | Omic  | Rank | Biomarker ID | Biomarker name                        | Omic  |
| 1    | MIMAT0000416 | hsa-mir-1-3p        | miRNA | 1    | cg15024277   | BEX3                                  | DNA   |
| 2    | MIMAT0004926 | hsa-mir-708-5p      | miRNA | 2    | cg20371266   | CHRND                                 | DNA   |
| 3    | MIMAT0004518 | hsa-mir-16-2-3p     | miRNA | 3    | cg22373770   | N/A                                   | DNA   |
| 4    | MIMAT0009451 | hsa-mir-1976        | miRNA | 4    | cg05165025   | MIDEAS,RP5-1021I20.1                  | DNA   |
| 5    | MIMAT0000080 | hsa-mir-24-3p       | miRNA | 5    | cg16503259   | N/A                                   | DNA   |
| 6    | DBC1         | BRINP1              | mRNA  | 6    | cg20253855   | CUX1                                  | DNA   |
| 7    | cg12676289   | CTD-2201E9.2,SEMA5A | DNA   | 7    | cg17237063   | RBMS3-AS3,RBMS3                       | DNA   |
| 8    | cg22777724   | HOXB2,HOXB-AS1      | DNA   | 8    | cg15275625   | N/A                                   | DNA   |
| 9    | cg26681383   | CACNA2D3            | DNA   | 9    | RNF126P1     | RNF126P1                              | mRNA  |
| 10   | cg09313705   | HOXB2,HOXB-AS1      | DNA   | 10   | TTY14        | TTY14                                 | mRNA  |
| 11   | cg20152430   | HOXB-AS3,HOXB3      | DNA   | 11   | C4orf45      | SPMIP2                                | mRNA  |
| 12   | LGALS2       | LGALS2              | mRNA  | 12   | SGCZ         | SGCZ                                  | mRNA  |
| 13   | MAGEA10      | MAGEA10             | mRNA  | 13   | NAA11        | NAA11                                 | mRNA  |
| 14   | MDH1B        | MDH1B               | mRNA  | 14   | cg00661753   | PTPRA                                 | DNA   |
| 15   | FOXH1        | FOXH1               | mRNA  | 15   | BET3L        | TRAPP3L                               | mRNA  |
| 16   | YBX2         | YBX2                | mRNA  | 16   | ZDHHC1       | ZDHHC1                                | mRNA  |
| 17   | PCDHAC2      | PCDHAC2             | mRNA  | 17   | G6PC         | G6PC1                                 | mRNA  |
| 18   | LOC644172    | LOC644172           | mRNA  | 18   | GPR52        | GPR52                                 | mRNA  |
| 19   | CTTNBP2      | CTTNBP2             | mRNA  | 19   | cg12472597   | CTC-1337H24.4,CLCF1,RAD9A,AP003419.11 | DNA   |
| 20   | DMRTA2       | DMRTA2              | mRNA  | 20   | cg11867599   | ABHD18,MFSD8                          | DNA   |
| 21   | TEX15        | TEX15               | mRNA  | 21   | CCL3L1       | CCL3L1                                | mRNA  |
| 22   | SYBU         | SYBU                | mRNA  | 22   | cg00020474   | N/A                                   | DNA   |
| 23   | BICC1        | BICC1               | mRNA  | 23   | cg14302471   | LINC00689                             | DNA   |
| 24   | FOXA3        | FOXA3               | mRNA  | 24   | ENC1         | ENC1                                  | mRNA  |
| 25   | cg27452922   | N/A                 | DNA   | 25   | PRR5-ARHGAP8 | PRR5-ARHGAP8                          | mRNA  |
| 26   | cg11241756   | H2BP2               | DNA   | 26   | cg14985891   | CASQ2                                 | DNA   |
| 27   | cg20197814   | HECW2               | DNA   | 27   | cg07971493   | MAP3K15                               | DNA   |
| 28   | cg00334056   | LEMD2               | DNA   | 28   | cg08316083   | ATP8B3                                | DNA   |
| 29   | cg22968622   | DND1P1              | DNA   | 29   | MIMAT0000707 | hsa-mir-363-3p                        | miRNA |
| 30   | cg08836615   | N/A                 | DNA   | 30   | KCNC2        | KCNC2                                 | mRNA  |

N/A indicates the biomarker name for the corresponding ID is not available.

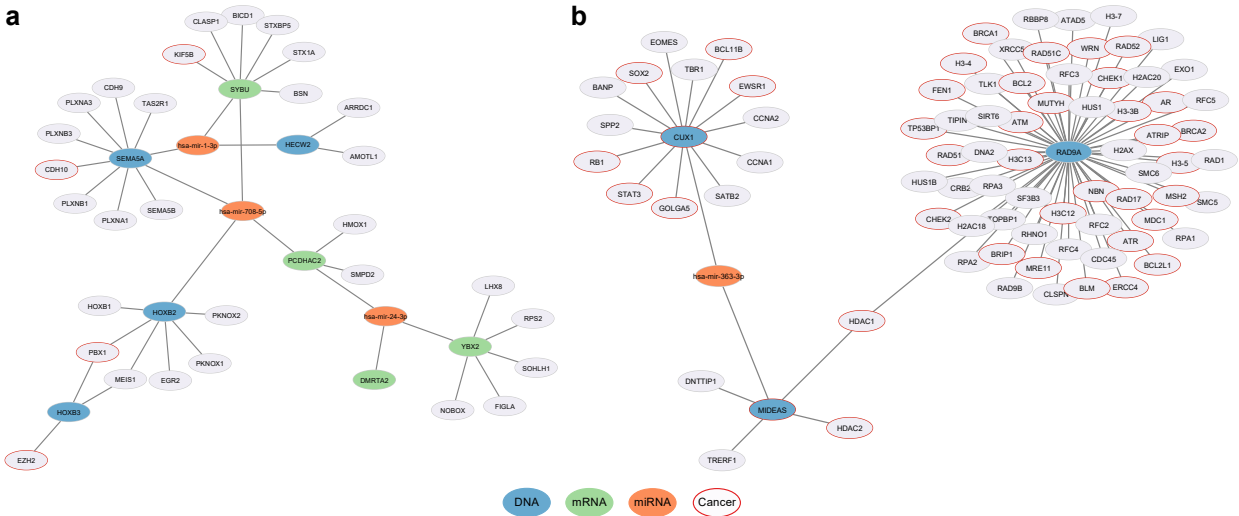


**Fig. 5. Known partners of selected top biomarkers. a,** Results for the BLCA dataset. **b,** Results for the LGG dataset. Direct protein-protein interactions are recovered for DNA and mRNA omics. For the miRNA omics, known mRNA targets are recovered from starBase<sup>57</sup>. The different omic categories from which the biomarkers originate are indicated as blue (DNA), green (mRNA) and orange (miRNA). Known cancer-related genes from the Cancer Gene Census database, OncoKB<sup>TM</sup> Cancer Gene List, and the Network Cancer Genome are circled in red<sup>58-60</sup>.

feature spaces. Our HeteroGATomics is a GAT-based method enhanced with heterogeneous graphs to integrate multiomics data for cancer diagnosis. To construct these heterogeneous graphs, we employ a novel dual-view representation leveraging feature and patient similarity networks. HeteroGATomics utilizes a joint feature selection approach using a multi-agent system, effectively addressing the high dimensionality of the feature space.

Experimental results demonstrate that the standalone joint feature selection module of HeteroGATomics consistently



outperforms baseline feature selection methods and achieves competitive performance in the remaining cases (Supplementary Section S2). This suggests that employing an effective joint feature selection strategy across multiple modalities can outperform independent feature selection for each modality. Another key innovation of HeteroGATomics is the construction of heterogeneous graphs through our proposed dual-view representation. Leveraging these heterogeneous graphs has significantly enhanced the performance of HeteroGATomics over the feature selection module across all datasets in the experiments, particularly in terms of AUROC. Furthermore, experiments show that, on average, HeteroGATomics outperforms both conventional and state-of-the-art multiomics integration methods in cancer classification tasks across six evaluation metrics.

Ablation studies demonstrate that each component of the heterogeneous graphs positively impacts HeteroGATomics' performance compared to homogeneous graphs. This highlights the importance of leveraging auxiliary information inherent in multiomics datasets for cancer classification and HeteroGATomics' superiority when utilizing this information compared to other methods. Additionally, ablation studies reveal the advantage of training HeteroGATomics with multiple omics over fewer omics, reflecting the complementary information each omic provides to the model. HeteroGATomics is flexible, enabling the integration of additional omics that contribute to understanding cancer progression.

Interpretability is another crucial aspect of this study, essential for building trust in HeteroGATomics. We enhance interpretability through a biomarker identification process that explains which genes and features have the most significant impact on the classification of BLCA and LGG cancers. HeteroGATomics successfully predicts known biomarkers in each cohort, including known genes involved in tumorigenesis, diagnosis and/or treatment. We show via interaction networks that several biomarkers are associated and highlight important functions that are or could be targeted for therapy (e.g. DNA damage repair pathways in LGG). HeteroGATomics also identifies genes that were not previously studied in LGG or BLCA, with several known oncogenes in other cancers. Examples of novel therapy target candidates for LGG include ion channels genes *CHRND* and *KCNC2*. For BLCA, the top five miRNAs biomarkers can progress miRNA pools used for diagnosis and prognosis. We highlight two network clusters of either interconnected markers, or markers that share common interactors. These may well be highlighting key regulatory processes, where a single process can be disrupted in multiple way to achieve oncogenicity. HeteroGATomics also uncovers non protein coding genes of interest like pseudogenes including long non coding RNAs (lncRNAs, e.g. *RNF126P1* and *TTY14* in LGG). Their relevance in cancer has been more recently investigated. For instance dysregulation of lncRNAs has been shown to impact glioma development<sup>61</sup>.

Future work can leverage the flexible architecture of HeteroGATomics to incorporate additional modalities beyond biological omics, such as medical imaging and electronic health records. These can serve as attributes in patient similarity networks, allowing the model to learn the interconnected structure of multiple modalities and potentially further boost its performance. Moreover, the dual-view representation concept in HeteroGATomics is broadly applicable, extending beyond the specific problem and datasets used in this study. This approach can be adapted to tabular-structured datasets and applied across various fields beyond cancer genomics, wherever explicit/implicit meaningful relationships among features exist. HeteroGATomics, similar to many studies, requires patients to have all omics available and cannot handle patients with one or more omics missing. Enabling HeteroGATomics to learn from missing omics will improve its performance in multiomics datasets.

## Methods

### Notations

The important notations used in this paper are provided in Supplementary Table S1.

### Data collection and preprocessing

We incorporate DNA methylation measured from the Illumina Infinium HumanMethylation450 BeadChip platform into our analysis, with 90% of the probes from the HumanMethylation27 data present. For gene expression RNAseq, we select the IlluminaHiSeq pancan normalized version. In this modality, values were transformed using *Log2* mean-normalized per gene across all TCGA patients. Then, only the converted data specific to the cohort of interest was extracted. Moreover, we include miRNA obtained from the IlluminaHiSeq system, where values were *Log2*-transformed. More details can be found at the UCSC Xena platform<sup>23</sup>.

After collecting the datasets, we perform four preprocessing steps to clean and prepare the data for machine learning models. First, only patients with information in all omic modalities are retained. Second, features with missing values in each omic are removed. Third, all features in each omic are normalized to the range [0, 1] using min-max scaling<sup>62</sup>. Fourth, features with little discriminatory power are eliminated by filtering out those with variance below a specific threshold. The threshold is set at 0.04 for DNA and mRNA, while miRNA is exempt from filtering due to its limited number of features. All datasets in the experiments use this variance threshold. Table 1 shows the number of features for each dataset and omic modality after the completion of each phase.

## Joint feature selection

The high dimensionality of multiomics datasets results in many irrelevant and redundant features, challenging GNNs to learn meaningful representations and perform classification tasks. Thus, a feature selection method is needed to identify representative features. We propose a joint feature selection strategy to mitigate the curse of dimensionality by modeling intra- and cross-omic interactions, instead of applying separate feature selection to each omic modality.

HeteroGATomics employs the ant colony optimization algorithm (ACO), a robust multi-agent framework, for conducting joint feature selection. The rationale for selecting ACO over other MAS is driven by several factors: (1) leveraging global communication through a distributed long-term memory system to facilitate information exchange among agents and enhance the decision-making process, (2) the inherently parallel nature of its implementation, leading to a substantial reduction in computational time, and (3) its balanced global and local search capabilities, supporting efficient exploration and the adoption of greedy exploitation approaches<sup>63,64</sup>.

**Multomics data representation.** The input omics can be represented as interconnected graphs, with each graph corresponding to a distinct omic, as illustrated in Supplementary Fig. S6.

Consider a labelled omic  $D^m = \langle \mathbf{X}^m, \mathbf{Y} \rangle$ , where  $\mathbf{X}^m \in \mathbb{R}^{N \times d_m}$  represents a matrix of  $N$  patients with  $d_m$  features, and  $\mathbf{Y} \in \mathbb{R}^{N \times C}$  denotes patient labels for  $C$  classes, represented using one-hot encoding. Formally, each omic can be formulated as an undirected weighted graph  $\mathcal{G}^m = (\mathcal{V}^m, \mathcal{E}^m, p_m)$ , where  $\mathcal{V}^m$  is a set of  $d_m$  nodes indicating features in omic  $m$ , and  $\mathcal{E}^m \in \mathcal{V}^m \times \mathcal{V}^m$  is a set of edges connecting these features. Additionally,  $\mathcal{G}$  includes  $p_m$ , denoting the relative importance of omic  $m$ . Graph weights are calculated by the absolute value of the Pearson correlation coefficient<sup>27</sup> between pairs of nodes. Due to the high dimensionality and numerous correlated features within omics, utilizing a sparse graph in the feature selection algorithm accelerates training, reduces memory usage, and enhances computational efficiency. Therefore, we retain a percentage of edges with weights below the threshold  $\theta_f$ . Furthermore, the relevance of each feature is assessed using ANOVA and assigned to the corresponding graph node.

The ACO algorithm relies on desirability, characterized by pheromone levels, that reflects the attractiveness of solutions and guides the algorithm towards near-optimal solutions. We use two key desirability values: (1) the node desirability value  $\tau_v^m$ , indicating the significance of feature  $v$  relative to other features in omic  $m$ ; and (2) the edge desirability value  $\tau_e^m$ , showing the importance of the edge  $e$  between two features within omic  $m$ . These values are initialized to small constant values  $c_\gamma$  and  $c_\epsilon$ , and are assigned to each node and edge, respectively.

**ACO for joint feature selection.** Following data representation, we use ACO for joint feature selection (see Supplementary Algorithm 1), involving an iterative improvement process with several key steps in each iteration. First,  $N_A$  agents are randomly distributed across different graph nodes within each omic. Then, each agent independently constructs its solution by traversing interconnected graphs using iterative “state transition rules”. These rules guide agents to select unchosen features probabilistically or greedily, biased by desirability strengths and the relevance and correlation values of target nodes and edges. Following the construction step, solutions are evaluated using a proposed “fitness function”. The highest-quality solution in the current iteration is retained as the best-found solution.

Once all solutions are evaluated, we modify desirability values on nodes and edges using the “desirability updating rules”. This involves reducing the strengths of desirability values by a constant parameter and depositing additional value on promising nodes and edges, based on their attractiveness during solution construction. Furthermore, the relative importance of each omic, denoted as  $p_m$ , is updated using an “omic importance updating rule”, which allocates higher probability to omics whose features contributed more to the agents’ solutions. These steps repeat for a predefined number of iterations. Finally, to construct reduced-dimensionality multiomics, we retain the top  $B$  features selected by a weighted combination of node desirability and relevance value.

**State transition rules.** Each agent constructs a solution by navigating interconnected graphs and selecting features using either a probabilistic or greedy rule. In the greedy rule, the transition from feature  $i$  to feature  $j$  within omic  $m$  for agent  $a$  is defined as:

$$f_j^m = \arg \max_{j \in \mathcal{J}_i^m(a)} \left[ \eta_1(f_j^m) + \tau_j^m + \tau_{ij}^m - \eta_2(f_j^m) \right] \text{ if } q \leq q_0, \quad (1)$$

where  $\mathcal{J}_i^m(a)$  represents the set of feasible features yet to be selected by agent  $a$  in omic  $m$ ,  $\tau_j^m$  is the desirability value of node  $j$  in omic  $m$ ,  $\tau_{ij}^m$  is the desirability value on the edge between nodes  $i$  and  $j$  in omic  $m$ ,  $q$  is a random number in the interval  $[0, 1]$ , and  $q_0 \in [0, 1]$  is a constant parameter. In equation (1),  $\eta_1(\cdot)$  assesses feature relevance, while  $\eta_2(\cdot)$  measures the average correlation between a new feature and those previously selected by agent  $a$ . A lower  $\eta_2(\cdot)$  value increases the likelihood of selecting a promising feature.

In the probabilistic rule, used when  $q > q_0$ , an agent is allowed to probabilistically explore other omics to select any feature based on its probability value. Given that an agent  $a$  is currently placed in omic  $m$ , the next omic  $m'$ , which can be equal to the current omic, is randomly selected from the set of omics  $\mathcal{M}^{19}$ . This selection is based on the set of probabilities  $\mathcal{P} = \{p_1, p_2, \dots, p_M\}$ , indicating the relative importance of each omic. Once the next omic is chosen, the probability of transitioning to feature  $j$  from omic  $m'$  is given by:

$$\Pr(f_j^{m'} | f_i^m) = \frac{\eta_1(f_j^{m'}) + \tau_j^{m'} - \eta_2(f_j^{m'})}{\sum_{v \in \mathcal{J}_i^{m'}(a)} [\eta_1(f_v^{m'}) + \tau_v^{m'} - \eta_2(f_v^{m'})]}. \quad (2)$$

In equation (2), the exclusion of edge desirability values simplifies the model and reduces computation time.

**Fitness function.** The fitness function evaluates the quality of solutions, reflecting their proximity to desired objectives. To evaluate the quality of solution  $S(a)$  constructed by agent  $a$ , we propose the following quantitative measure:

$$\text{fitness}(S(a)) = \frac{1}{3} [Q(S(a)) + R(S(a))], \quad (3)$$

where

$$R(S(a)) = \text{mean} \left( \sum_{v \in \mathcal{S}_v(a)} \text{rel}(f_v) \right) - \text{mean} \left( \sum_{(v,u) \in \mathcal{S}_e(a)} |\text{corr}(f_v, f_u)| \right), \quad (4)$$

$Q(S(a))$  quantifies the classifier's performance on the subset of selected features  $S(a)$ ,  $\mathcal{S}_v(a)$  is the subset of all features selected by agent  $a$  in its solution  $S(a)$ , and  $\mathcal{S}_e(a)$  is the subset of edges within the agent's solution. In Equation (3),  $R(\cdot)$  is a regularization term that penalizes solutions with irrelevant and redundant features, encouraging agents to find more informative and relevant subsets.

**Desirability updating rules.** These rules aim to enhance the desirability values associated with nodes and edges identified in high-quality solutions. The update process for node and edge desirability values occurs after all agents have constructed their solutions and are calculated by the following equations:

$$\tau_i^m = (1 - \rho_v) \tau_i^m + \rho_v \left[ \frac{\text{count}_v(\{f_i^m\})}{\text{count}_v(\mathcal{S}_v)} + [\Delta \tau_i^m]^{\text{best}} \right], \quad (5)$$

$$\tau_{ij}^m = (1 - \rho_e) \tau_{ij}^m + \rho_e \left[ \frac{\text{count}_e(\{f_i^m, f_j^m\})}{\text{count}_e(\mathcal{S}_e)} + [\Delta \tau_{ij}^m]^{\text{best}} \right], \quad (6)$$

where parameters  $\rho_v, \rho_e \in (0, 1]$  are the decay coefficients for node and edge desirability values, respectively, the functions  $\text{count}_v(\cdot)$  and  $\text{count}_e(\cdot)$  determine the number of times a subset of features and edges has been selected, respectively,  $\mathcal{S}_v$  denotes all selected features in the current iteration, and  $\mathcal{S}_e$  represents all selected edges in the current iteration. In equations (5) and (6),  $[\Delta \tau_i^m]^{\text{best}}$  and  $[\Delta \tau_{ij}^m]^{\text{best}}$  add the fitness value of the best-found solution in the current iteration if the respective feature or edge is selected in that solution; otherwise, they are zero. The desirability updating rules operate similarly to a reinforcement learning scheme, where better solutions receive higher reinforcement<sup>63</sup>.

**Omic importance updating rule.** This rule enhances the significance of omics containing informative features for agents in subsequent iterations and is adapted from ref.<sup>19</sup>.

### GAT architecture for heterogeneous graphs

After feature selection reduces feature dimensionality, we construct a heterogeneous graph for each omic. This graph is automatically generated, incorporating extensive structural information inherent in tabular omics for downstream tasks. Following this, a GAT encodes each heterogeneous graph, effectively representing node information. The powerful attention mechanism in the GAT architecture prioritizes important nodes and edges, which is beneficial for omics data where specific genes influence

biological processes or disease mechanisms. This focus on key elements in GAT enhances performance compared to other GNN architectures<sup>13,15,65</sup>. After encoding each heterogeneous graph, a single-layer neural network performs label prediction. We combine predictions from multiple omics into a tensor representing cross-omics label correlations, which is then processed through a VCDN for final prediction. Supplementary Algorithm 2 presents the pseudo-code for the proposed architecture.

**Heterogeneous graph construction.** For each omic, we construct a heterogeneous graph by combining a feature similarity network with a patient similarity network (see Fig. 1b). The *feature similarity network*, deriving from the feature selection phase, consists of nodes representing selected features and edges denoting the correlations between them. Node attributes are defined by their relevance, desirability, and corresponding values from the input omics, while edge weights are assigned based on the desirability and correlation between nodes. Complementing this, we construct the *patient similarity network* where nodes represent individual patients, and edges denote correlations between them. These correlations, quantified using the absolute Pearson correlation coefficient, serve as edge weights. Only edges with weights above a specified threshold,  $\theta_s$ , are maintained, which filters for the most significant patient correlations and results in a more manageable and relevant graph structure.

These two networks, indicating two distinct node types (patients and features), are interconnected to form a comprehensive heterogeneous graph encompassing three specific relations: “*patient-similar-patient*”, “*feature-similar-feature*”, and “*feature-attribute-patient*”. Each relation in the heterogeneous graph offers unique insights: “*patient-similar-patient*” reveals shared disease characteristics among patients; “*feature-similar-feature*” highlights the correlated dynamics of features in biological processes; and “*feature-attribute-patient*” provides key understanding of how individual features impact patient outcomes. This approach of relation-aware representation in the graph allows for capturing more detailed information, reflecting the diverse characteristics of the target nodes in omics datasets.

Formally, a heterogeneous graph is defined as  $\mathcal{G}_H^m = (\mathcal{V}^m, \mathcal{E}^m, \mathcal{O}, \mathcal{R})$ . Here,  $\mathcal{V}^m$  represents the set of nodes, each mapped to a node type via the function  $\phi(v_i) \rightarrow \mathcal{O}$  for  $v_i \in \mathcal{V}^m$ . The set of edges  $\mathcal{E}^m$  is denoted with a corresponding edge type mapping function  $\psi(v_i, u_j) \rightarrow \mathcal{R}$  for each edge  $(v_i, u_j) \in \mathcal{E}^m$  and relation  $r \in \mathcal{R}$ <sup>65</sup>.  $\mathcal{O}$  denotes the set of node types, and  $\mathcal{R}$  denotes the set of edge types or relations.

**Representation learning and label prediction.** HeteroGATomics employs multiple GAT layers to encode omic-specific heterogeneous graphs, where each GAT within a layer is tailored to a specific relation type (as illustrated in Fig. 1c). For a given heterogeneous graph  $\mathcal{G}_H^m$ , the goal of representation learning is to develop functions  $f_1 : \mathcal{V}_1^m \rightarrow \mathbb{R}^{d_h}$ ,  $f_2 : \mathcal{V}_1^m \rightarrow \mathbb{R}^{d_h}$ , and  $f_3 : \mathcal{V}_2^m \rightarrow \mathbb{R}^{d_h}$  which map the nodes corresponding to each of the three relations into a  $d_h$ -dimensional embedding space. Node types are split into two disjoint sets,  $\mathcal{V}^m = \mathcal{V}_1^m \cup \mathcal{V}_2^m$ , where  $\mathcal{V}_1^m \cap \mathcal{V}_2^m = \emptyset$ . When a node is the destination of several relations, their corresponding representations are aggregated. The HeteroGATomics encoder stacks multiple layers of three individual GATs, each encoding source nodes for a specific relation  $r$ , as follows:

$$\mathbf{H}_r^{(l+1)} = \mathbf{A}_r^{(l)} \mathbf{H}_r^{(l)} \mathbf{W}_r^{(l)\top}, \quad (7)$$

where  $\mathbf{H}_r^{(l)} \in \mathbb{R}^{N_r \times d_r^{(l)}}$  is the source node representation matrix in the  $l$ th layer for relation  $r$ ,  $N_r$  denotes the number of source nodes in relation  $r$ ,  $d_r^{(l)}$  is the hidden dimensional size of each source node in  $l$ th layer, and  $\mathbf{A}_r^{(l)}$  is the attention score matrix for relation  $r$ . In equation (7),  $\mathbf{W}_r^{(l)} \in \mathbb{R}^{d_r^{(l+1)} \times d_r^{(l)}}$  is the learnable weight matrix, where  $d_r^{(l+1)}$  represents the hidden dimension in layer  $l+1$ , and  $(\cdot)^\top$  indicates transposition. Node representations initially originate from the input node attribute matrix  $\mathbf{H}_r^{(0)} = \mathbf{X}_r$ , where  $\mathbf{X}_r \in \mathbb{R}^{N_r \times d_r^{(0)}}$ , and  $d_r^{(0)}$  is the dimensionality of each input source node. The GAT calculates the normalized attention scores  $\alpha_{ruv}^{(l)}$  of the attention score matrix  $\mathbf{A}_r^{(l)}$  between each pair of nodes  $u$  and  $v$  in relation  $r$  as follows:

$$\alpha_{ruv}^{(l)} = \frac{\exp\left(\sigma\left(\mathbf{a}_{rs}^{(l)\top} \mathbf{W}_{rs}^{(l)} \mathbf{h}_{ru}^{(l)} + \mathbf{a}_{rd}^{(l)\top} \mathbf{W}_{rd}^{(l)} \mathbf{h}_{rv}^{(l)} + \mathbf{a}_{re}^{(l)\top} \mathbf{W}_{re}^{(l)} \mathbf{e}_{ruv}\right)\right)}{\sum_{k \in \mathcal{N}(u)} \exp\left(\sigma\left(\mathbf{a}_{rs}^{(l)\top} \mathbf{W}_{rs}^{(l)} \mathbf{h}_{ru}^{(l)} + \mathbf{a}_{rd}^{(l)\top} \mathbf{W}_{rd}^{(l)} \mathbf{h}_{rk}^{(l)} + \mathbf{a}_{re}^{(l)\top} \mathbf{W}_{re}^{(l)} \mathbf{e}_{ruk}\right)\right)}, \quad (8)$$

where  $\mathbf{h}_{ru}^{(l)} \in \mathbb{R}^{d_r^{(l)}}$  and  $\mathbf{h}_{rv}^{(l)} \in \mathbb{R}^{d_r^{(l)}}$  denote the representations of nodes  $u$  and  $v$  in layer  $l$ , respectively,  $\mathbf{e}_{ruv}$  indicates the edge attributes between nodes  $u$  and  $v$  in relation  $r$ ,  $\mathbf{a}_{rs}^{(l)}$ ,  $\mathbf{a}_{rd}^{(l)}$ , and  $\mathbf{a}_{re}^{(l)}$  are the trainable attention vectors to weigh source, destination, and edge attributes, correspondingly, and  $\mathcal{N}(u)$  indicates the direct neighbor set of node  $u$  in the graph. In equation (8),  $\sigma(\cdot)$  represents LeakyReLU non-linearity function, and  $\exp(\cdot)$  denotes the standard exponential function.

To stabilize the attention mechanism learning process, multi-head attention<sup>15</sup> is widely utilized. This scheme involves combining the outputs of  $K$  distinct attention mechanisms to form the final node representations, as follows:

$$\mathbf{H}_r^{(l+1)} = \frac{1}{K} \sum_{k=1}^K \mathbf{A}_{rk}^{(l)} \mathbf{H}_r^{(l)} \mathbf{W}_{rk}^{(l)\top}. \quad (9)$$

Once each heterogeneous graph is mapped into node embeddings through attention layers, a single-layer neural network uses them for omic-specific label prediction. We optimize trainable parameters via backpropagation to minimize the cross-entropy loss function across all training patients, as defined:

$$\mathcal{L}_m = \sum_{(\mathbf{x}_i^m, \mathbf{y}_i) \in \mathcal{D}_{tr}^m} \text{CE}_m(\mathbf{y}_i, \hat{\mathbf{y}}_i^m), \quad (10)$$

where

$$\text{CE}_m(\mathbf{y}_i, \hat{\mathbf{y}}_i^m) = - \sum_{c=1}^C y_{ic} \log \frac{\exp(\hat{y}_{ic}^m)}{\sum_{j=1}^C \exp(\hat{y}_{ij}^m)}, \quad (11)$$

$\mathcal{D}_{tr}^m$  represents all the training patients in omic  $m$ ,  $\mathbf{x}_i^m$  is the  $i$ th training patient with its corresponding label  $\mathbf{y}_i$ ,  $\hat{\mathbf{y}}_i^m$  indicates the class probabilities predicted by the GAT model, and function  $\text{CE}_m(\cdot)$  denotes the cross-entropy loss. In equation (11),  $C$  is the number of classes, and  $\hat{y}_{ic}^m$  represents the  $c$ th element in the predicted probability vector.

We utilize VCDN, which integrates different omic-specific label predictions, to perform final prediction. This network excels at learning both intra- and cross-omic correlations within the label space, thereby enhancing performance across several tasks<sup>4,66</sup>. For each patient, we create a cross-omic discovery tensor by integrating predicted class probabilities from various omics. This tensor is then reshaped into a vector of dimension  $C^M$ . VCDN, a fully connected network, uses this vector as input to make the final prediction. The cross-entropy loss function is employed for training VCDN<sup>4</sup>.

## Data availability

The three datasets used in this study, BLCA, LGG, and RCC, are all publicly accessible through the UCSC Xena platform (<https://xenabrowser.net/datapages/>). To facilitate reproducibility, the processed datasets are available in the GitHub repository ([https://github.com/SinaTabakhi/HeteroGATomics/tree/main/raw\\_data](https://github.com/SinaTabakhi/HeteroGATomics/tree/main/raw_data)).

## Code availability

The source code and implementation details of HeteroGATomics are publicly available in the GitHub repository (<https://github.com/SinaTabakhi/HeteroGATomics>) and are archived in the Zenodo repository<sup>67</sup> (<https://doi.org/10.5281/zenodo.13119631>) under the MIT License. An interactive Google Colab demonstration is available at: [https://colab.research.google.com/github/SinaTabakhi/HeteroGATomics/blob/main/HeteroGATomics\\_demo.ipynb](https://colab.research.google.com/github/SinaTabakhi/HeteroGATomics/blob/main/HeteroGATomics_demo.ipynb).

## Acknowledgements

S.T. is supported by the University of Sheffield Faculty of Engineering Research Scholarship (grant number 199256787). I.S. and C.V. are supported by the Medical Research Council (MRC) grant MR/V010948/1.

## Author contributions

S.T. and H.L. conceived and designed the study. S.T. developed the models and performed the experiments under the supervision of H.L. S.T. implemented the biomarker identification algorithm. C.V. designed the biological interpretation of the results under the guidance of I.S. S.T. and C.V. wrote the manuscript. H.L. performed critical revisions of the article. All authors reviewed and edited the manuscript.

## Competing interests

The authors declare no competing interests.

## References

1. Steyaert, S. *et al.* Multimodal data fusion for cancer biomarker discovery with deep learning. *Nat. Mach. Intell.* **5**, 351–362 (2023).
2. Acosta, J. N., Falcone, G. J., Rajpurkar, P. & Topol, E. J. Multimodal biomedical AI. *Nat. Med.* **28**, 1773–1784 (2022).
3. Karczewski, K. J. & Snyder, M. P. Integrative omics for health and disease. *Nat. Rev. Genet.* **19**, 299–310 (2018).
4. Wang, T. *et al.* MOGONET integrates multi-omics data using graph convolutional networks allowing patient classification and biomarker identification. *Nat. Commun.* **12**, 3445 (2021).
5. Cantini, L. *et al.* Benchmarking joint multi-omics dimensionality reduction approaches for the study of cancer. *Nat. Commun.* **12**, 124 (2021).
6. Schulte-Sasse, R., Budach, S., Hnisz, D. & Marsico, A. Integration of multiomics data with graph convolutional networks to identify new cancer genes and their associated molecular mechanisms. *Nat. Mach. Intell.* **3**, 513–526 (2021).
7. Li, M. M., Huang, K. & Zitnik, M. Graph representation learning in biomedicine and healthcare. *Nat. Biomed. Eng.* **6**, 1353–1369 (2022).
8. Picard, M., Scott-Boyer, M.-P., Bodein, A., Périn, O. & Droit, A. Integration strategies of multi-omics data for machine learning analysis. *Comput. Struct. Biotechnol. J.* **19**, 3735–3746 (2021).
9. Peng, C., Zheng, Y. & Huang, D.-S. Capsule network based modeling of multi-omics data for discovery of breast cancer-related genes. *IEEE/ACM Trans. Comput. Biol. Bioinform.* **17**, 1605–1612 (2019).
10. Rappoport, N. & Shamir, R. NEMO: cancer subtyping by integration of partial multi-omic data. *Bioinformatics* **35**, 3348–3356 (2019).
11. Sun, D., Wang, M. & Li, A. A multimodal deep neural network for human breast cancer prognosis prediction by integrating multi-dimensional data. *IEEE/ACM Trans. Comput. Biol. Bioinform.* **16**, 841–850 (2018).
12. Hamilton, W. L., Ying, R. & Leskovec, J. Representation learning on graphs: methods and applications. Preprint at <https://arxiv.org/abs/1709.05584> (2018).
13. Forster, D. T. *et al.* BIONIC: biological network integration using convolutions. *Nat. Methods* **19**, 1250–1261 (2022).
14. Ektefaie, Y., Dasoulas, G., Noori, A., Farhat, M. & Zitnik, M. Multimodal learning with graphs. *Nat. Mach. Intell.* **5**, 340–350 (2023).
15. Veličković, P. *et al.* Graph attention networks. In *International Conference on Learning Representations (ICLR)*, (2018).
16. Zitnik, M. *et al.* Current and future directions in network biology. Preprint at <https://arxiv.org/abs/2309.08478> (2023).
17. Tabakhi, S., Suvon, M. N. I., Ahadian, P. & Lu, H. Multimodal learning for multi-omics: a survey. *World Sci. Annu. Rev. Artif. Intell.* **1**, 2250004 (2023).
18. El-Manzalawy, Y., Hsieh, T.-Y., Shivakumar, M., Kim, D. & Honavar, V. Min-redundancy and max-relevance multi-view feature selection for predicting ovarian cancer survival using multi-omics data. *BMC Med. Genom.* **11**, 19–31 (2018).
19. Tabakhi, S. & Lu, H. Multi-agent feature selection for integrative multi-omics analysis. In *Annual International Conference of the IEEE Engineering in Medicine and Biology Society*, 1638–1642 (IEEE, 2022).
20. Ruiz, C., Ren, H., Huang, K. & Leskovec, J. High dimensional, tabular deep learning with an auxiliary knowledge graph. In *Advances in Neural Information Processing Systems (NeurIPS)*, (2023).
21. Xu, H. *et al.* GripNet: graph information propagation on supergraph for heterogeneous graphs. *Pattern Recognit.* **133**, 108973 (2023).
22. Chandak, P., Huang, K. & Zitnik, M. Building a knowledge graph to enable precision medicine. *Sci. Data* **10**, 67 (2023).
23. Goldman, M. J. *et al.* Visualizing and interpreting cancer genomics data via the Xena platform. *Nat. Biotechnol.* **38**, 675–678 (2020).
24. The Cancer Genome Atlas Research Network. Comprehensive molecular characterization of urothelial bladder carcinoma. *Nature* **507**, 315 (2014).
25. The Cancer Genome Atlas Research Network. Comprehensive, integrative genomic analysis of diffuse lower-grade gliomas. *N. Engl. J. Med.* **372**, 2481–2498 (2015).
26. Chen, F. *et al.* Multilevel genomics-based taxonomy of renal cell carcinoma. *Cell Rep.* **14**, 2476–2489 (2016).
27. Theodoridis, S. & Koutroumbas, K. *Pattern Recognition* (Elsevier Science, 2008).

28. Ho, T. K. Random decision forests. In *Proceedings of the International Conference on Document Analysis and Recognition*, vol. 1, 278–282 (IEEE, 1995).
29. Hoerl, A. E. & Kennard, R. W. Ridge regression: biased estimation for nonorthogonal problems. *Technometrics* **12**, 55–67 (1970).
30. Chen, T. & Guestrin, C. XGBoost: a scalable tree boosting system. In *Proceedings of the ACM SIGKDD International Conference on Knowledge Discovery and Data Mining*, 785–794 (ACM, 2016).
31. Lv, Z., Wang, T., Cao, X., Sun, M. & Qu, Y. The role of receptor-type protein tyrosine phosphatases in cancer. *Precis. Med. Sci.* **12**, 57 – 66 (2023).
32. Griffin, M., Khan, R., Basu, S. & Smith, S. Ion channels as therapeutic targets in high grade gliomas. *Cancers* **12**, 3068 (2020).
33. Xu, Y. *et al.* Screening critical genes associated with malignant glioma using bioinformatics analysis. *Mol. Med. Rep.* **16**, 6580–6589 (2017).
34. Li, J. *et al.* Identification of the nerve-cancer cross-talk-related prognostic gene model in head and neck squamous cell carcinoma. *Front. Oncol.* **11**, 788671 (2021).
35. Yamashita, H. *et al.* On a FOX hunt: functions of FOX transcriptional regulators in bladder cancer. *Nat. Rev. Urol.* **14**, 98–106 (2017).
36. Liu, J. *et al.* HOXB2 is a putative tumour promotor in human bladder cancer. *Anticancer. Res.* **39**, 6915–6921 (2019).
37. Yuan, Z. *et al.* Comprehensive pan-cancer analysis of YBX family reveals YBX2 as a potential biomarker in liver cancer. *Front. Immunol.* **15**, 1382520 (2024).
38. Deng, L. *et al.* A novel and sensitive DNA methylation marker for the urine-based liquid biopsies to detect bladder cancer. *BMC Cancer* **22**, 510 (2022).
39. Mantere, T. *et al.* Case-control analysis of truncating mutations in DNA damage response genes connects TEX15 and FANCD2 with hereditary breast cancer susceptibility. *Sci. Rep.* **7**, 681 (2017).
40. Verma, S. *et al.* Melanoma antigen family A (MAGE A) as promising biomarkers and therapeutic targets in bladder cancer. *Cancers* **16**, 246 (2024).
41. Das, S., Hayden, J., Sullivan, T. & Rieger-Christ, K. The roles of miRNAs in predicting bladder cancer recurrence and resistance to treatment. *Int. J. Mol. Sci.* **24**, 964 (2023).
42. Sequeira, J. P. *et al.* OncoUroMiR: circulating miRNAs for detection and discrimination of the main urological cancers using a ddPCR-based approach. *Int. J. Mol. Sci.* **24**, 13890 (2023).
43. Lee, T.-Y. *et al.* Anti-microRNA-1976 as a novel approach to enhance chemosensitivity in XAF1+ pancreatic and liver cancer. *Biomedicines* **11**, 1136 (2023).
44. Khodadadi-Jamayran, A. *et al.* Prognostic role of elevated mir-24-3p in breast cancer and its association with the metastatic process. *Oncotarget* **9**, 12868 (2018).
45. Tan, Z. *et al.* Dysregulation and prometastatic function of glycosyltransferase C1GALT1 modulated by cHP1BP3/miR-1-3p axis in bladder cancer. *J. Exp. & Clin. Cancer Res.* **41**, 228 (2022).
46. Song, T. *et al.* miR-708 promotes the development of bladder carcinoma via direct repression of Caspase-2. *J. Cancer Res. Clin. Oncol.* **139**, 1189–1198 (2013).
47. Ware, A. P., Kabekkodu, S. P., Chawla, A., Paul, B. & Satyamoorthy, K. Diagnostic and prognostic potential clustered mirnas in bladder cancer. *3 Biotech* **12**, 173 (2022).
48. Zhang, J. *et al.* miR-1-3p contributes to cell proliferation and invasion by targeting glutaminase in bladder cancer cells. *Cell. Physiol. Biochem.* **51**, 513–527 (2018).
49. Ferri, A., Stagni, V. & Barilà, D. Targeting the DNA damage response to overcome cancer drug resistance in glioblastoma. *Int. J. Mol. Sci.* **21**, 4910 (2020).
50. Biswas, H., Makinwa, Y. & Zou, Y. Novel cellular functions of atr for therapeutic targeting: embryogenesis to tumorigenesis. *Int. J. Mol. Sci.* **24**, 11684 (2023).
51. Cascio, C. L. *et al.* Nonredundant, isoform-specific roles of HDAC1 in glioma stem cells. *JCI Insight* **6** (2021).
52. Mondal, B. *et al.* The histone deacetylase complex MiDAC regulates a neurodevelopmental gene expression program to control neurite outgrowth. *Elife* **9**, e57519 (2020).

53. Feng, F. *et al.* CUX1 facilitates the development of oncogenic properties via activating Wnt/ $\beta$ -catenin signaling pathway in glioma. *Front. Mol. Biosci.* **8**, 705008 (2021).
54. Górnicki, T. *et al.* Role of RBMS3 novel potential regulator of the EMT phenomenon in physiological and pathological processes. *Int. J. Mol. Sci.* **23**, 10875 (2022).
55. Ruan, X. *et al.* RBMS3-induced circHECTD1 encoded a novel protein to suppress the vasculogenic mimicry formation in glioblastoma multiforme. *Cell Death & Dis.* **14**, 745 (2023).
56. Nishiyama, H., Gill, J. H., Pitt, E., Kennedy, W. & Knowles, M. A. Negative regulation of G(1)/S transition by the candidate bladder tumour suppressor gene DBCCR1. *Oncogene* **20**, 2956–2964 (2001).
57. Li, J.-H., Liu, S., Zhou, H., Qu, L.-H. & Yang, J.-H. starBase v2. 0: decoding miRNA-ceRNA, miRNA-ncRNA and protein–RNA interaction networks from large-scale CLIP-Seq data. *Nucleic Acids Res.* **42**, D92–D97 (2014).
58. Sondka, Z. *et al.* COSMIC: a curated database of somatic variants and clinical data for cancer. *Nucleic Acids Res.* **52**, D1210–D1217 (2024).
59. Chakravarty, D. *et al.* OncoKB: a precision oncology knowledge base. *JCO Precis. Oncol.* **2017**, PO.17.00011 (2017).
60. Repana, D. *et al.* The Network of Cancer Genes (NCG): a comprehensive catalogue of known and candidate cancer genes from cancer sequencing screens. *Genome Biol.* **20**, 1–12 (2019).
61. Wu, X. *et al.* The involvement of long non-coding RNAs in glioma: from early detection to immunotherapy. *Front. Immunol.* **13**, 897754 (2022).
62. You, J., Ma, X., Ding, Y., Kochenderfer, M. J. & Leskovec, J. Handling missing data with graph representation learning. In *Advances in Neural Information Processing Systems* (NeurIPS, 2020).
63. Dorigo, M. & Gambardella, L. M. Ant colony system: a cooperative learning approach to the traveling salesman problem. *IEEE Trans. Evol. Comput.* **1**, 53–66 (1997).
64. Dorigo, M. & Blum, C. Ant colony optimization theory: a survey. *Theor. Comput. Sci.* **344**, 243–278 (2005).
65. Hamilton, W. L. *Graph Representation Learning* (Morgan & Claypool Publishers, 2020).
66. Wang, L., Ding, Z., Tao, Z., Liu, Y. & Fu, Y. Generative multi-view human action recognition. In *Proceedings of the IEEE/CVF International Conference on Computer Vision*, 6212–6221 (IEEE, 2019).
67. Tabakhi, S., Vandermeulen, C., Sudbery, I. & Lu, H. HeteroGATomics v1.0.0. Zenodo <https://doi.org/10.5281/zenodo.13119631> (2024).



# Supplementary Information

## S1 Notations

**Table S1. Notations and descriptions.**

| <b>Notation</b>  | <b>Description</b>   |
|--|--|
| $\mathbf{a}_{rs}^{(l)}, \mathbf{a}_{rd}^{(l)}, \mathbf{a}_{re}^{(l)}$        | Attention vectors to weigh source, destination, and edge attributes for relation $r$ in $l$ th layer                                 |
| $\mathbf{A}_r^{(l)}$   | Attention score matrix for relation $r$ in $l$ th layer  |
| $c_{\mathcal{V}}, c_{\mathcal{E}}$   | Initial constant values for node and edge desirabilities   |
| $\mathcal{D}^m = \langle \mathbf{X}^m, \mathbf{Y} \rangle$                   | Labelled omic dataset with patients $\mathbf{X}^m \in \mathbb{R}^{N \times d_m}$ and labels $\mathbf{Y} \in \mathbb{R}^{N \times C}$ |
| $\mathbf{e}_{ruv}$   | Edge attributes between nodes $u$ and $v$ in relation $r$  |
| $\eta_1, \eta_2$   | Heuristic information for feature relevance and average feature correlation  |
| $\mathcal{G}^m = (\mathcal{V}^m, \mathcal{E}^m, p_m)$                        | Undirected weighted graph with nodes $\mathcal{V}^m$ , edges $\mathcal{E}^m$ , and omic importance $p_m$                             |
| $\mathcal{G}_H^m = (\mathcal{V}^m, \mathcal{E}^m, \mathcal{O}, \mathcal{R})$ | Heterogeneous graph with nodes $\mathcal{V}^m$ , edges $\mathcal{E}^m$ , and corresponding types $\mathcal{O}, \mathcal{R}$          |
| $\mathbf{H}_r^{(l)}$   | Source node representations for relation $r$ in $l$ th layer   |
| $\mathcal{J}_i^m(a)$   | Feasible features to be selected by agent $a$ in omic $m$  |
| $\mathcal{M}$  | Set of omics   |
| $\mathcal{N}(v)$   | Neighbors of node $v$  |
| $\mathcal{P} = \{p_1, p_2, \dots, p_M\}$                                     | Set of omic importance values  |
| $q, q_0 \in [0, 1]$  | Random number and control parameter in the probabilistic/greedy rules  |
| $\rho_{\mathcal{V}}, \rho_{\mathcal{E}}, \rho_{\mathcal{M}} \in (0, 1]$      | Node, edge, and omic importance decay coefficients   |
| $\mathcal{S}_{\mathcal{V}}, \mathcal{S}_{\mathcal{E}}$                       | Selected features and edges in the current iteration   |
| $\mathcal{S}(a)$   | Solution constructed by agent $a$  |
| $\mathcal{S}_{\mathcal{V}}(a), \mathcal{S}_{\mathcal{E}}(a)$                 | Selected features and edges by agent $a$ within its solution $\mathcal{S}(a)$  |
| $\tau_v^m, \tau_e^m = \tau_{vu}^m$   | Desirability values for node $v$ and edge $e = (v, u)$ in omic $m$   |
| $\theta_f, \theta_s$   | Thresholds to discard edges in feature and patient similarity networks   |
| $\mathbf{W}_r^{(l)}$   | Weight matrix for relation $r$ in $l$ th layer   |
| $\mathbf{X}_r \in \mathbb{R}^{N_r \times d_r^{(0)}}$                         | Input node attributes for relation $r$   |
| $\hat{\mathbf{y}}_i^m$   | Class probabilities predicted by the GAT model in omic $m$   |

Vectors are denoted by lowercase boldface letters, matrices by uppercase boldface, and sets by calligraphic letters.

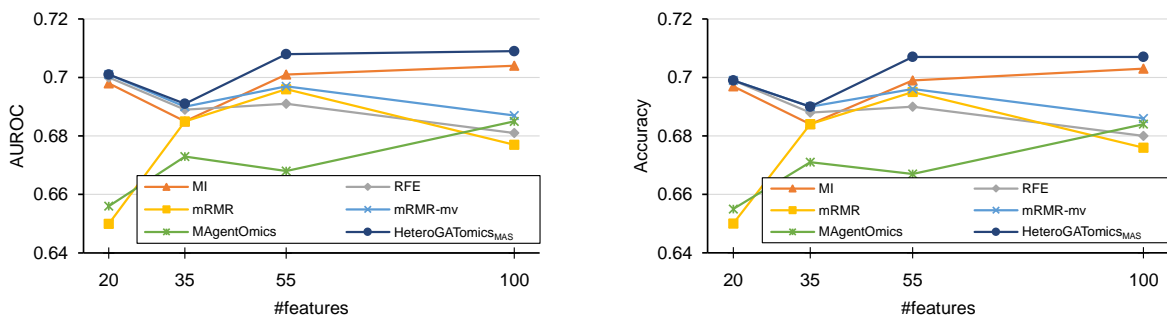
## S2 Feature selection performance comparison

We compare the feature selection module of HeteroGATomics (HeteroGATomics<sub>MAS</sub>) with five baseline feature selection methods: mutual information (MI)<sup>1</sup>, recursive feature elimination (RFE)<sup>2</sup>, minimal-redundancy–maximal-relevance (mRMR)<sup>3</sup>, minimal-redundancy–maximal-relevance multi-view (mRMR-mv)<sup>4</sup>, and multi-agent architecture for multi-omics (MAgentOmics)<sup>5</sup>. Notably, mRMR-mv and MAgentOmics are specifically designed for joint feature selection within multiomics datasets. To evaluate the performance of MI, RFE, and mRMR, we concatenate the selected features from each modality to serve as the input for a classifier.

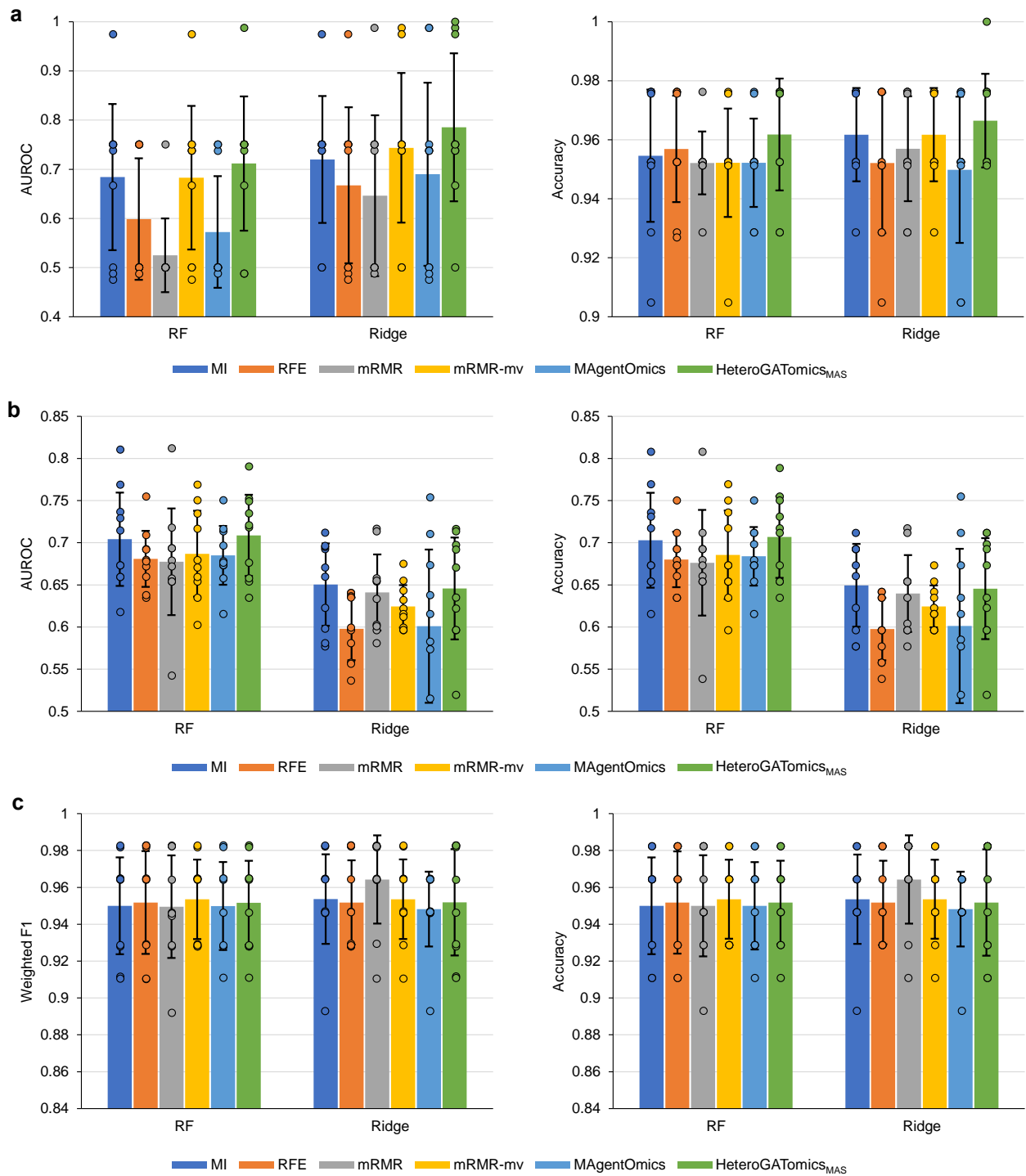
Figure S1 presents the classification results of different feature selection methods on LGG using a random forest (RF)<sup>6</sup> classifier, with logarithmically spaced selected feature sizes. HeteroGATomics<sub>MAS</sub> has consistently outperformed other methods in terms of AUROC and accuracy. MI, a univariate method, achieves the second-highest performance, even against multivariate methods. This suggests that LGG may contain individual features with significant independent predictive power, and the complex interactions identified by multivariate methods may not significantly enhance performance. This finding highlights the effectiveness of HeteroGATomics<sub>MAS</sub> in identifying discriminative features despite its multivariate nature. Interestingly, both AUROC and accuracy metrics yield remarkably similar trends across all methods, indicating a well-balanced trade-off between true and false positive rates.

Figure S2 further validates the generalizability of HeteroGATomics<sub>MAS</sub> by comparing its performance across three datasets. The figure compares results for 100 selected features from each modality, evaluated with two classifiers, RF and Ridge regression (Ridge)<sup>7</sup>. On BLCA, HeteroGATomics<sub>MAS</sub> outperforms all baselines across both evaluation criteria with both classifiers, surpassing the best-reported baseline by 2.8% with RF and 4.2% with Ridge in AUROC (Fig. S2a). For LGG, HeteroGATomics<sub>MAS</sub> continues to excel in identifying high-quality features, leading to superior evaluation metrics with RF (Fig. S2b). While MI slightly outperforms HeteroGATomics<sub>MAS</sub> by less than 0.5% in AUROC and accuracy with Ridge, HeteroGATomics<sub>MAS</sub> remains the top performer in both metrics when using RF, even surpassing Ridge’s results. RCC, known for its relatively straightforward nature in the classification task<sup>8</sup>, sees all methods achieving high performance in both metrics with both classifiers (Fig. S2c). HeteroGATomics<sub>MAS</sub> remains competitive on RCC when using RF, with mRMR only outperforming it under Ridge. Additionally, we observe that the efficacy of a given feature selection technique is highly dependent on the dataset. mRMR, for example, is the superior method for RCC, yet it significantly underperforms compared to baselines for BLCA when Ridge is used.

These analyses highlight HeteroGATomics<sub>MAS</sub>’s ability to effectively identify discriminative features across different datasets and classifiers.



**Fig. S1. Performance comparison of feature selection methods for random forest classification on the LGG dataset.** The averaged values from 10-fold cross-validation are reported for each metric. The x-axis represents logarithmically spaced selected feature sizes for each modality, while the y-axis displays AUROC (left) and accuracy (right). HeteroGATomics<sub>MAS</sub> denotes the feature selection module within HeteroGATomics.



**Fig. S2. Performance comparison of feature selection methods for random forest and Ridge classification (mean and standard deviation over 10-fold cross-validation).** **a**, Results for the BLCA dataset. **b**, Results for the LGG dataset. **c**, Results for the RCC dataset. The results are presented based on 100 selected features for each modality. The vertical bars show the mean, the black lines represent error bars indicating plus/minus one standard deviation, and each dot is a model's performance on each fold. HeteroGATomics<sub>MAS</sub> denotes the feature selection module within HeteroGATomics.

### S3 Additional analysis of identified biomarkers

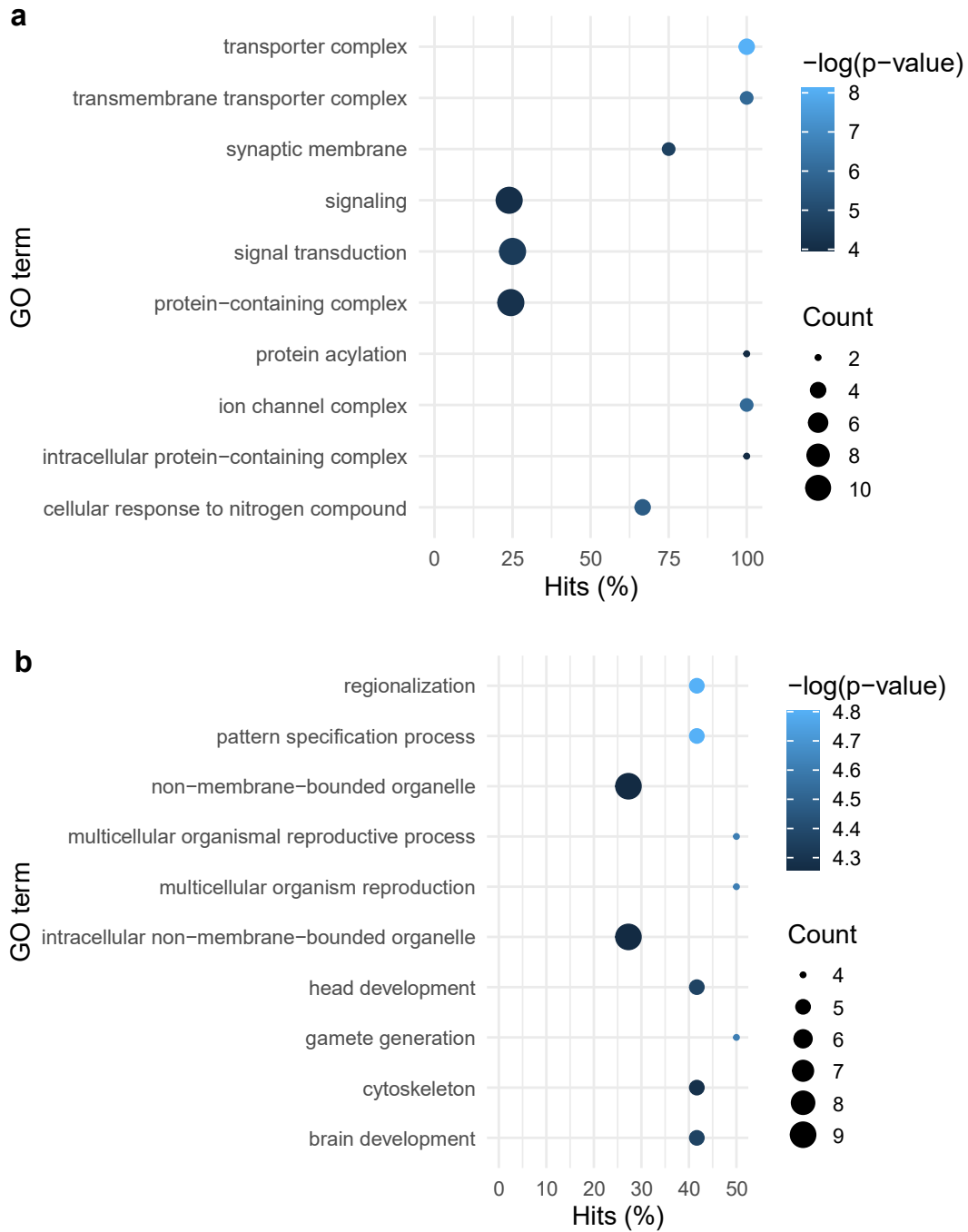


**Fig. S3. GO enrichment analysis of the top 30 biomarkers from the DNA and mRNA omics modalities. a,** Results for the LGG dataset. **b,** Results for the BLCA dataset. The y-axis shows the top 10 most significant GO category terms, while the x-axis represents the percentage of biomarkers belonging to each GO category.

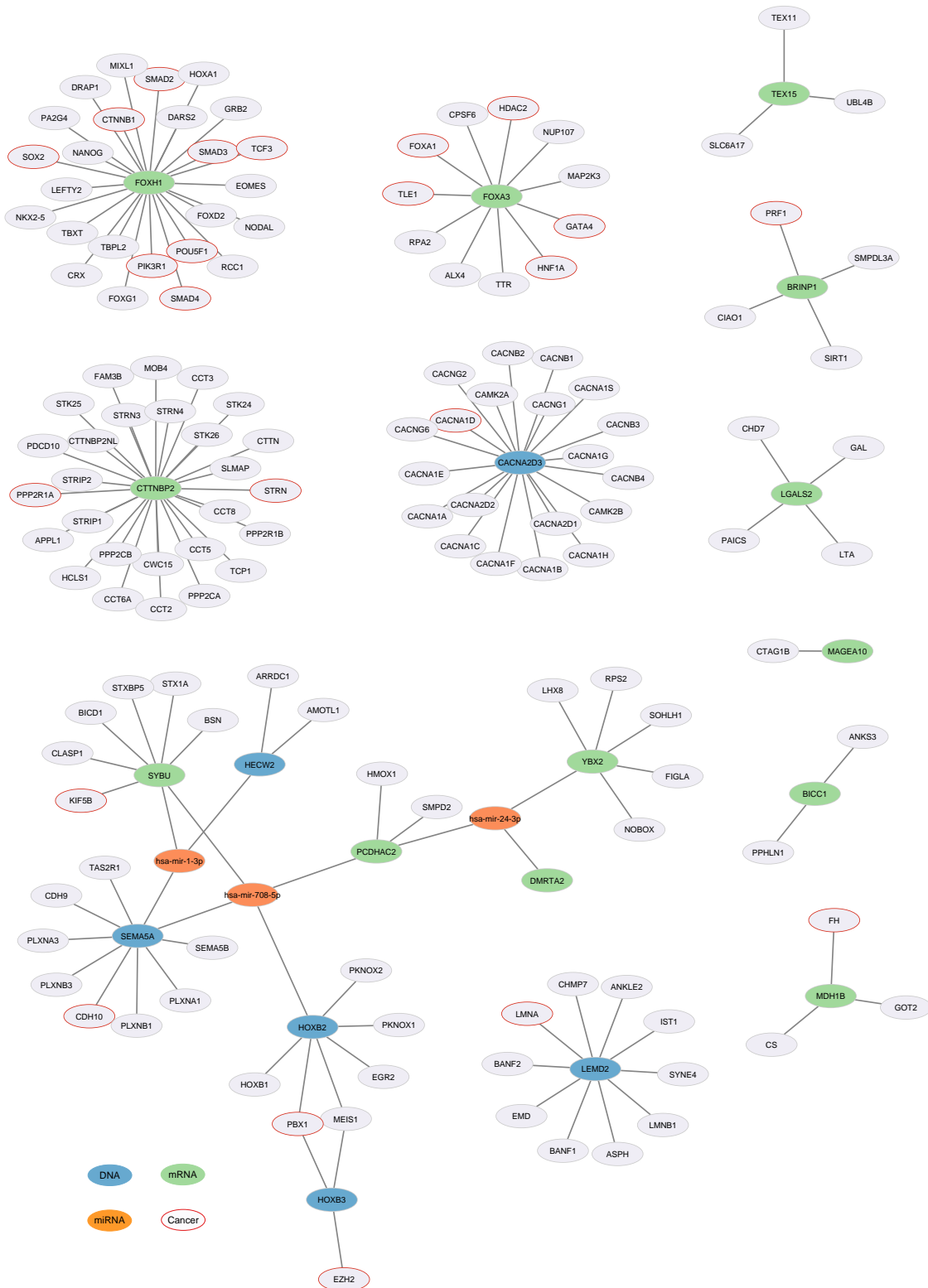


**Fig. S4. Interaction network of top 30 biomarkers with known partners for the BLCA dataset.** Only known direct interactions from protein-protein interaction databases are recovered for DNA and mRNA omics. For miRNA omics, known mRNA targets are recovered from starBase<sup>9</sup>. The different omics categories from which the biomarkers originate are indicated as blue (DNA), green (mRNA) and orange (miRNA). Known cancer-related genes are encircled in red.

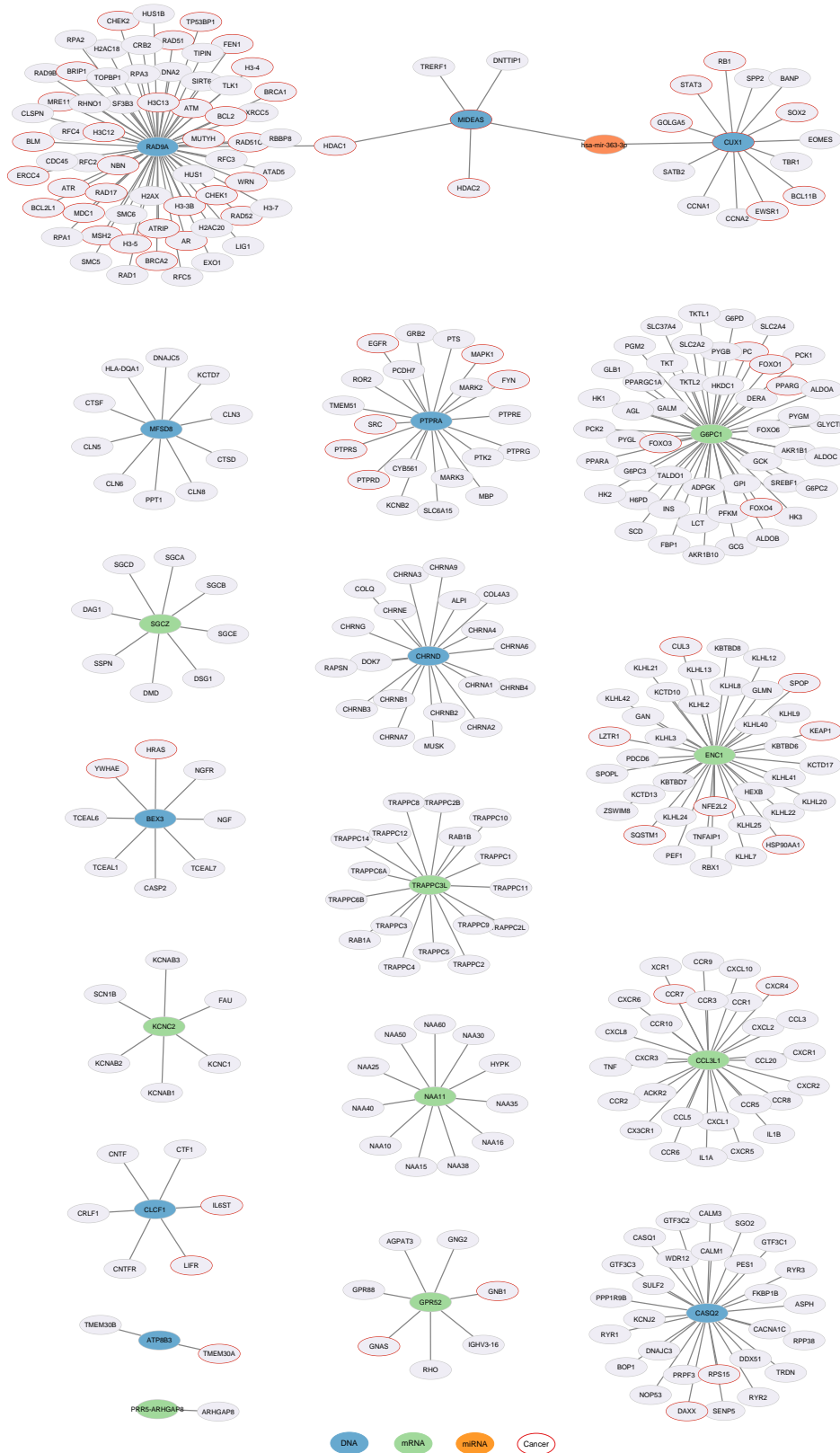


**Fig. S5. Interaction network of top 30 biomarkers with known partners for the LGG dataset.** Only known direct interactions from protein-protein interaction databases are recovered for DNA and mRNA omics. For miRNA omics, known mRNA targets are recovered from starBase<sup>9</sup>. The different omics categories from which the biomarkers originate are indicated as blue (DNA), green (mRNA) and orange (miRNA). Known cancer-related genes are encircled in red.

## S4 Materials and methods

### S4.1 Algorithms and extended architecture

To explain the HeteroGATomics architecture, detailed pseudo-code for each module is provided. Specifically, Algorithm 1 presents the feature selection module, while Algorithm 2 presents the GAT module of HeteroGATomics. Furthermore, Fig. S6 illustrates the feature space representation of multiomics data employed by MAS within HeteroGATomics for joint feature selection.

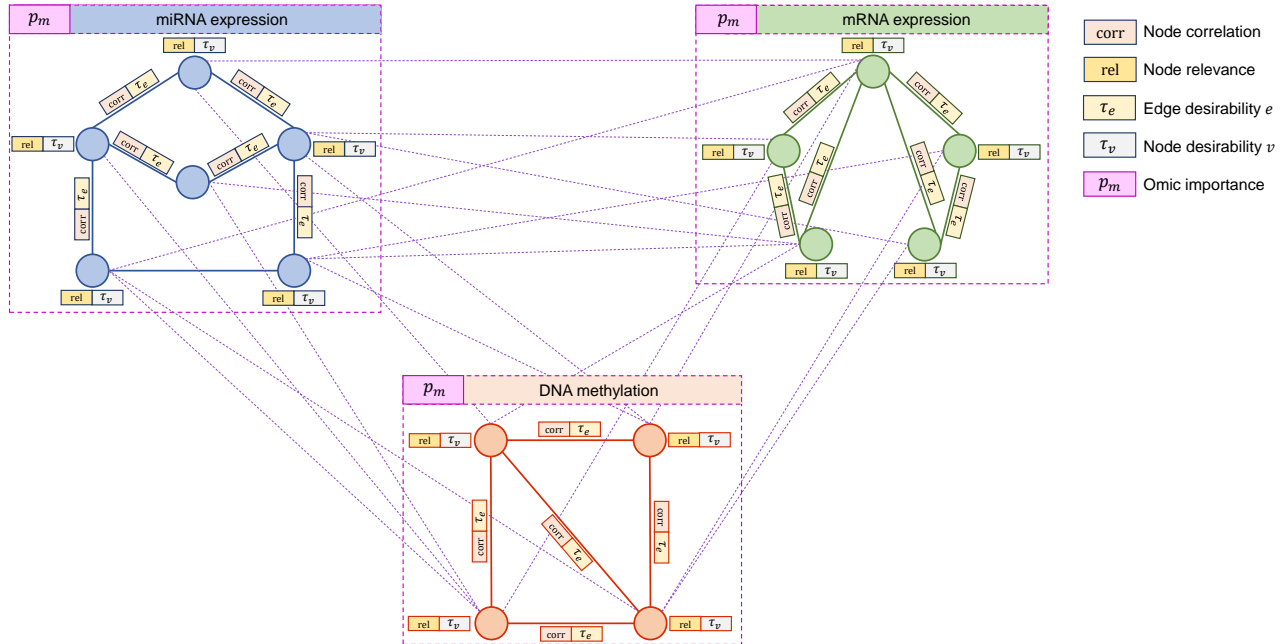


**Fig. S6. Multiomics representation for joint feature selection.** Each graph represents a specific omic modality. Nodes within the graph represent individual features, and edges indicate the similarity between pairs of these features. All omics are connected together to enable interactions across different omics.

---

**Algorithm 1** HeteroGATomics – Joint Feature Selection Module.

---

**Input**

$D = \langle (\mathbf{X}^1, \mathbf{X}^2, \dots, \mathbf{X}^M), \mathbf{Y} \rangle$ : multiomics dataset with  $M$  omics  
 $T$ : predefined number of iterations  
 $N_A$ : the number of agents per modality

**Output**

$D' = \langle (\mathbf{Z}^1, \mathbf{Z}^2, \dots, \mathbf{Z}^M), \mathbf{Y} \rangle$ : multiomics dataset with reduced feature dimensions  
 $\{\tau_v^m, \tau_{vu}^m\}_{m=1}^M$ : node and edge desirabilities

```
1: for  $m = 1$  to  $M$  do
2:   Compute node relevance  $\text{rel}(f_v^m)$ 
3:   Compute node pair correlation  $\text{corr}(f_v^m, f_u^m)$ 
4:   Initialize node desirability  $\tau_v^m(0) \leftarrow c_v$ 
5:   Initialize edge desirability  $\tau_{vu}^m(0) \leftarrow c_e$ 
6:   Initialize omic importance  $p_m \leftarrow \frac{1}{M}$ 
7:   Build a sparse graph by retaining edges with weights below the threshold  $\theta_f$ 
8: end for
9: for  $t = 1$  to  $T$  do
10:  for  $m = 1$  to  $M$  do
11:   for  $a = 1$  to  $N_A$  do
12:    Place agent  $a$  randomly on a unique node
13:    Build a solution by iteratively applying state transition rules from Eqs. (1) and (2)
14:    Evaluate the solution with the fitness function in Eq. (3)
15:   end for
16:  end for
17:  Retain the solution with the highest fitness as the best-found  $S(\text{best})$  in iteration  $t$ 
18:  Apply desirability updating rules to nodes and edges according to Eqs. (5) and (6)
19:  Apply omic importance updating rule
20: end for
21: Select the top  $B$  features using the weighted sum of node desirability and relevance value
22: Build multiomics dataset  $D'$  with the top  $B$  features
```

---

---

**Algorithm 2** HeteroGATomics – Graph Attention Network Module.

---

**Input**

$D' = \langle (\mathbf{Z}^1, \mathbf{Z}^2, \dots, \mathbf{Z}^M), \mathbf{Y} \rangle$ : multiomics dataset with  $M$  omics and reduced feature dimensions  
 $\{\tau_v^m, \tau_{vu}^m\}_{m=1}^M$ : node and edge desirabilities  
 $T_{\text{pre}}$ : the number of epochs for pre-training models  
 $T_{\text{train}}$ : the number of epochs for training models

**Output**

$\hat{\mathbf{y}} \in \mathbb{R}^N$ : final predicted labels

```
1: for  $m = 1$  to  $M$  do
2:   Construct patient similarity network from  $\mathbf{Z}^m$ 
3:   Construct feature similarity network using  $\tau_v^m, \tau_{vu}^m$ , and  $\mathbf{Z}^m$ 
4:   Construct heterogeneous graph  $G_H^m$  by combining feature and patient similarity networks
5: end for
6: for  $t = 1$  to  $T_{\text{pre}}$  do
7:  for  $m = 1$  to  $M$  do
8:   Apply GAT for representation learning on the graph  $G_H^m$  via Eq. (9)
9:   Predict omic-specific labels via a single-layer neural network on learned representations
10:  Optimize omic-specific model parameters by minimizing the cross-entropy loss according to Eq. (10)
11:  end for
12: end for
13: for  $t = 1$  to  $T_{\text{train}}$  do
14:  for  $m = 1$  to  $M$  do
15:   Apply GAT for representation learning on the graph  $G_H^m$  via Eq. (9)
16:   Predict omic-specific labels via a single-layer neural network on learned representations
17:  end for
18:  Create a cross-omic discovery tensor for each patient
19:  Predict final labels  $\hat{\mathbf{y}}$  with VCDN from the cross-modality discovery tensor
20:  Optimize VCDN parameters by minimizing the cross-entropy loss
21:  for  $m = 1$  to  $M$  do
22:   Optimize omic-specific model parameters by minimizing the cross-entropy loss according to Eq. (10)
23:  end for
24: end for
```

---



## S4.2 Biomarker identification with HeteroGATomics

HeteroGATomics facilitates the identification of key cancer biomarkers, enhancing our understanding of its decision-making process. This process is essential for interpreting the architecture's effectiveness and pinpointing the most informative features serving as cancer biomarkers. We leverage an ablation approach commonly used in deep learning-based methods for biomarker selection<sup>8,10,11</sup>. This approach involves systematically removing each feature to observe its impact on the model's performance. Specifically, for each feature within a given omic, we temporarily remove the feature by setting its value and its attributes (i.e., node relevance and desirability) to zero in both the feature and patient similarity networks. Then, we evaluate the model's classification performance on the test set without this feature. Features whose removal leads to the most significant decrease in classification performance are considered top biomarkers. This decrease indicates the feature's substantial impact on the model, highlighting its importance. We apply a 10-fold cross-validation strategy, indicating that the set of input features to the GAT module may vary across different folds. Therefore, we assess the model's classification performance for each feature in every fold. To rank features from each omic modality, we measure the cumulative reduction in classification performance, which is then normalized according to the frequency of their occurrences across all folds. To evaluate the performance of HeteroGATomics, we use AUROC for binary classification tasks in the BLCA and LGG datasets.

GO enrichment analyses are performed with Goseq in R, using GO biological process (GO BP), molecular function (MF), and cellular component (CC). The top 30 biomarkers for mRNA and DNA omic categories are used as enrichment sets with the remaining 300 biomarkers as the background set. Protein-protein interaction networks are generated in Cytoscape, using string-db<sup>12</sup> and ConsensusPathway<sup>13</sup> databases for known physical interactions. Only direct two-by-two interactions are used, with an interaction confidence of  $\geq 7$  for string-db and  $\geq 9.5$  for ConsensusPathway (reported as high confidence interactions). Known cancer-related genes are fetched from the Cancer Gene Census database<sup>14</sup>, OncoKB<sup>TM</sup> Cancer Gene List<sup>15</sup>, and the Network Cancer Genome<sup>16</sup>. Target mRNAs for miRNA biomarkers are inferred from starBase<sup>9</sup>, keeping only targets with at least one CLIP experiment evidence and predicted by at least two miRNA target predictor tools (e.g. miRanda and/or TargetScan).

## S4.3 Experimental setting

**Implementation.** HeteroGATomics has been developed using Python 3.10 and PyTorch Geometric 2.4.0 (ref.<sup>17</sup>), incorporating essential functionalities from PyTorch 2.1.0 (ref.<sup>18</sup>), scikit-learn 1.3.0 (ref.<sup>19</sup>), NumPy 1.26.0 (ref.<sup>20</sup>), pandas 2.1.1 (ref.<sup>21</sup>), and SciPy 1.11.3 (ref.<sup>22</sup>). The training process for the GAT module and VCDN utilizes the PyTorch Lightning 2.1.3 (ref.<sup>23</sup>). For the training of omic-specific encoders using the GAT module and the VCDN, the Adam optimizer<sup>24</sup> is employed with the StepLR learning rate scheduler strategy, which reduces the learning rate by a factor of 0.8 every 20 epochs. Each omic-specific encoder comprises a three-layer GAT model with hidden dimensions set to [100, 100, 50], incorporating LeakyReLU nonlinearity with a negative slope of 0.01 after each layer. The decoders for each omics type utilize a single-layer fully connected neural network to map the final 50-neuron hidden layer to the output labels. The omic-specific encoder-decoder pairs is pre-trained for 500 epochs, followed by a full training of the entire architecture for an additional 500 epochs. Hyperparameter optimization is guided by 10-fold cross-validation, with validation set performance informing the selection of optimal parameters. Detailed hyperparameter configurations are available in Section S5, Tables S2 and S3, and Fig. S7. We also conduct an execution time analysis presented in Section S6.

**Baselines.** We compare the performance of feature selection module of HeteroGATomics with five baseline methods: (1) MI<sup>1</sup> quantifies the dependency between two random variables, yielding a non-negative value that is often used to select features with the highest information shared with the target class; (2) RFE<sup>2</sup> recursively removes the least important features based on an estimator's weights, starting with all features and stopping at the desired number; (3) mRMR<sup>3</sup> selects features that have the highest relevance with the target class and are minimally redundant with each other, balancing the trade-off between relevance and redundancy; (4) mRMR-mv<sup>4</sup> is an adaption of mRMR to multiomics integration setting; (5) MAgentOmics<sup>5</sup> is an iterative improvement method that extends the ACO algorithm to work with multiomics data.

When performing baseline feature selection methods, we remove five features at each iteration in RFE, employ the recommended hyperparameter values for mRMR-mv as specified in its original paper, and use the values listed in Table S3 for MAgentOmics, ensuring a uniform comparison with HeteroGATomics' feature selection module. We utilize the scikit-feature package<sup>25</sup> for implementing mRMR, and scikit-learn for implementing MI and RFE.

For multiomics classification, we compare HeteroGATomics against eight baseline methods. For direct feature concatenation across all omics modalities, machine learning approaches including KNN<sup>1</sup>, MLP<sup>1</sup>, RF<sup>6</sup>, Ridge<sup>7</sup>, and XGBoost<sup>26</sup> are employed. mRMR-mv and MAgentOmics focus on joint feature selection, specifically tailored for multiomics data integration. MOGONET<sup>8</sup>, a supervised multiomics integration framework for classification tasks, leverages GCN for omic-specific patient classification and employs VCDN to combine initial predictions from each omics modality into a final label prediction.

For comparative analysis, we use scikit-learn for KNN, MLP, RF, and Ridge implementations, keeping to their default settings. Specifically, the MLP model is configured with 500 epochs in scikit-learn, while other parameters remain at their

default values. The XGBoost classifier is implemented using the XGBoost package<sup>26</sup>, with its default configurations. For MOGONET, we follow the hyperparameter recommendations from its original publication. To ensure a fair comparison, MOGONET is run for 500 epochs of pre-training for each omic-specific GCN, and then for an additional 500 epochs for training the entire architecture, similar to the HeteroGATomics setup.

### S5 Hyperparameter setting

We evaluate six hyperparameters of the GAT module within HeteroGATomics across various datasets, with results provided in Fig. S7. This analysis uses the average of evaluation metrics from a 10-fold cross-validation across the entire dataset, where, in each fold, the training set is split into training and validation sets at a 9:1 ratio. The results presented are the average values of the evaluation metrics derived from the validation sets. For binary classification tasks in the BLCA and LGG datasets, we utilize AUROC, while Weighted F1 is used for multi-class classification in the RCC dataset. The six evaluated hyperparameters include the number of attention heads, sparsity rate, dropout rate, pre-training learning rate (pre-training lr), training learning rate (training lr), and VCDN learning rate (VCDN lr). Table S2 summarizes the range of possible values for each hyperparameter and highlights the optimal values identified through the optimization process. To assess the impact of individual hyperparameters, each one is varied at a time while keeping the others constant.

For the HeteroGATomics<sub>MAS</sub> module, we primarily adopt the hyperparameter values recommended by the foundational ACO algorithm papers<sup>27-29</sup>, established through extensive studies. Furthermore, the sparsity rate for each modality within the feature selection module is carefully chosen to guarantee enough edges in the graph, enabling effective traversal by the agents. The common hyperparameter settings applied across all datasets are outlined in Table S3.

**Table S2. Dataset-specific hyperparameter configurations for HeteroGATomics.**

| Dataset | Number of heads | Sparsity rate               | Dropout rate                  | Pre-training lr               | Training lr                   | VCDN lr                       |
|---------|-----------------|-----------------------------|-------------------------------|-------------------------------|-------------------------------|-------------------------------|
|         | {2, 3, 4}       | { <b>0.80</b> , 0.85, 0.90} | { <b>0.0</b> , 0.1, 0.2, 0.3} | {0.050, <b>0.010</b> , 0.001} | {0.050, 0.010, <b>0.001</b> } | {0.050, <b>0.010</b> , 0.001} |
| BLCA    | 3               | 0.90                        | 0.0                           | 0.010                         | 0.001                         | 0.05                          |
| LGG     | 2               | 0.85                        | 0.3                           | 0.001                         | 0.001                         | 0.05                          |
| RCC     | 2               | 0.80                        | 0.0                           | 0.001                         | 0.001                         | 0.05                          |

Values in sets present the potential options for each hyperparameter, with the bolded value within each set marking the predetermined choice for that hyperparameter when varying another.

**Table S3. Common hyperparameter configurations for HeteroGATomics across datasets.**

| Module   | Hyperparameter                                 | Value          |
|--|--|----------------|
| HeteroGATomics <sub>MAS</sub>  | Number of iterations                           | 50             |
|  | Number of agents per omic                      | 10             |
|  | Initial node desirability ( $c_V$ )            | 0.2            |
|  | Initial edge desirability ( $c_E$ )            | 0.2            |
|  | Node decay coefficient ( $\rho_V$ )            | 0.1            |
|  | Edge decay coefficient ( $\rho_E$ )            | 0.1            |
|  | Omic importance decay coefficient ( $\rho_M$ ) | 0.1            |
|  | Number of selected features in each iteration  | 30             |
|  | Control parameter $q_0$                        | 0.8            |
| Sparsity rate for each omic in feature similarity network (DNA, mRNA, miRNA) | [0.9, 0.9, 0.8]                                |                |
| HeteroGATomics <sub>GAT</sub>  | Number of epochs for pre-training model        | 500            |
|  | Number of epochs for training model            | 500            |
|  | Number of layers                               | 3              |
|  | Hidden node dimensions for each layer          | [100, 100, 50] |

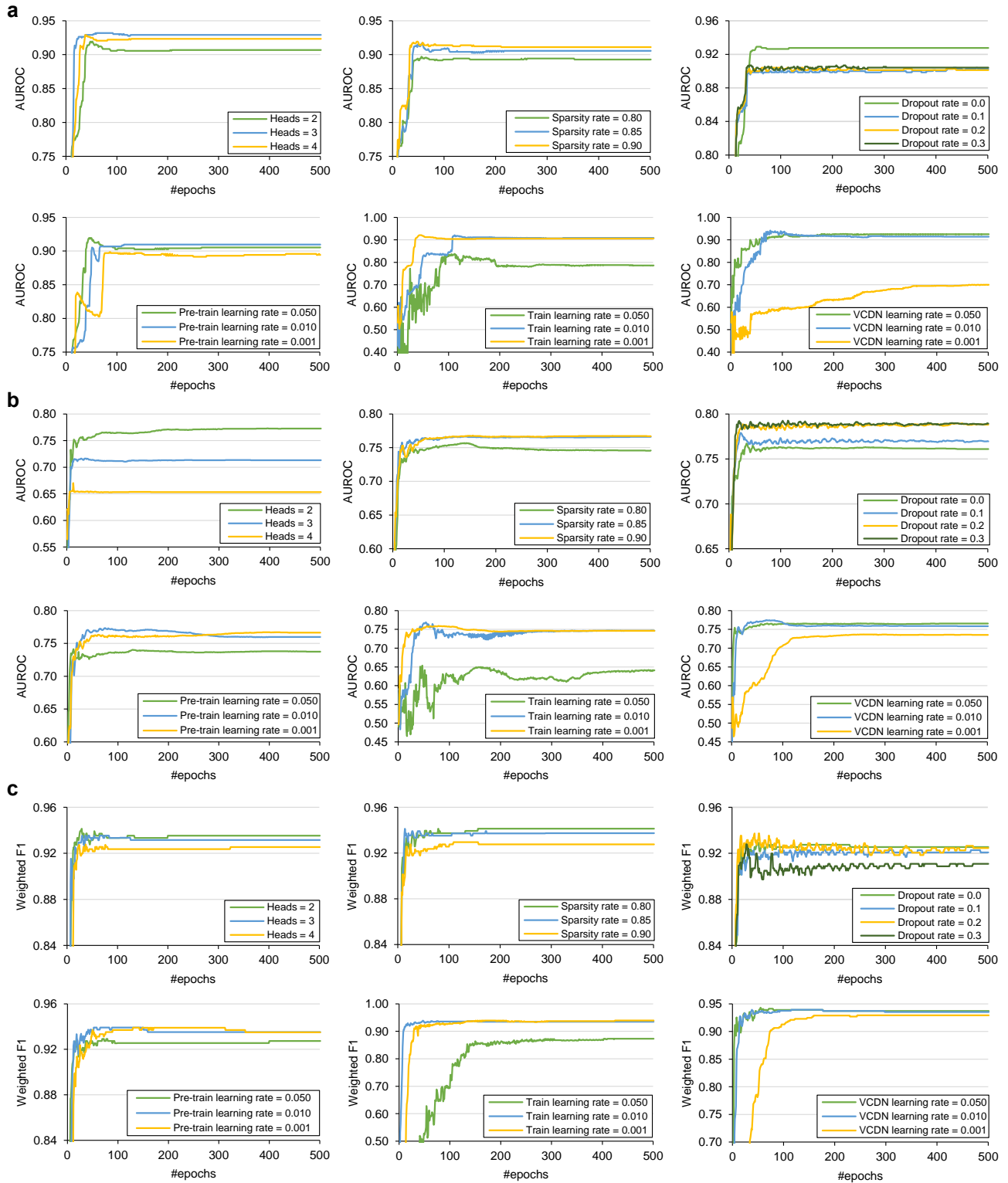


**Fig. S7. HeteroGATomics classification performance across datasets with different hyperparameter configurations. a,** Results for the BLCA dataset with AUROC. **b,** Results for the LGG dataset with AUROC. **c,** Results for the RCC dataset with Weighted F1. Averaged values from 10-fold cross-validation are presented. Each fold divides the training set into training and validation sets, with the respective evaluation metric reported for the validation set. The x-axis represents epochs, while the y-axis represents specific metric mentioned for each dataset.

## S6 Execution time analysis

We measure the execution time of two modules within HeteroGATomics: the HeteroGATomics<sub>MAS</sub> and HeteroGATomics<sub>GAT</sub> modules. In the HeteroGATomics<sub>MAS</sub> module, we exclusively evaluate the time required for feature selection, independent of the final classifier used. In the case of the HeteroGATomics<sub>GAT</sub>, the execution time involves various stages, including the creation of heterogeneous graphs, pre-training of each omic-specific GAT model, training each omic-specific GAT with the VCDN module (inactive for single modality), and testing the entire architecture. We utilize a CPU with 20 cores on the High-Performance Compute cluster, Stanage, at The University of Sheffield for the feature selection module and evaluate the GAT module using an NVIDIA GeForce RTX 4090 GPU. We adopt the hyperparameter configurations as detailed in Tables S2 and S3 for these evaluations, with the results presented in Fig. S8.

Figure S8a demonstrates that the execution time of the HeteroGATomics<sub>MAS</sub> remains relatively constant when varying the number of selected features. This behavior arises from the nature of the HeteroGATomics<sub>MAS</sub> as a feature-ranking technique<sup>2</sup>, where selecting additional features does not incur additional execution time. However, the figure also indicates that the total number of features in the dataset influences execution time, with higher feature counts leading to longer execution times.

In Fig. S8b, the execution time of the HeteroGATomics<sub>GAT</sub> is depicted across different combinations of omic modalities. It is observed that HeteroGATomics utilizing all omic modalities requires only 84 seconds, demonstrating high efficiency. The figure further reveals that minimal differences are observed between leveraging two or three omic modalities, suggesting that adding more omic modalities slightly increases execution time. The only exception is the single omic case, where the VCDN module remains inactive during training, leading to the expected decrease in execution time.

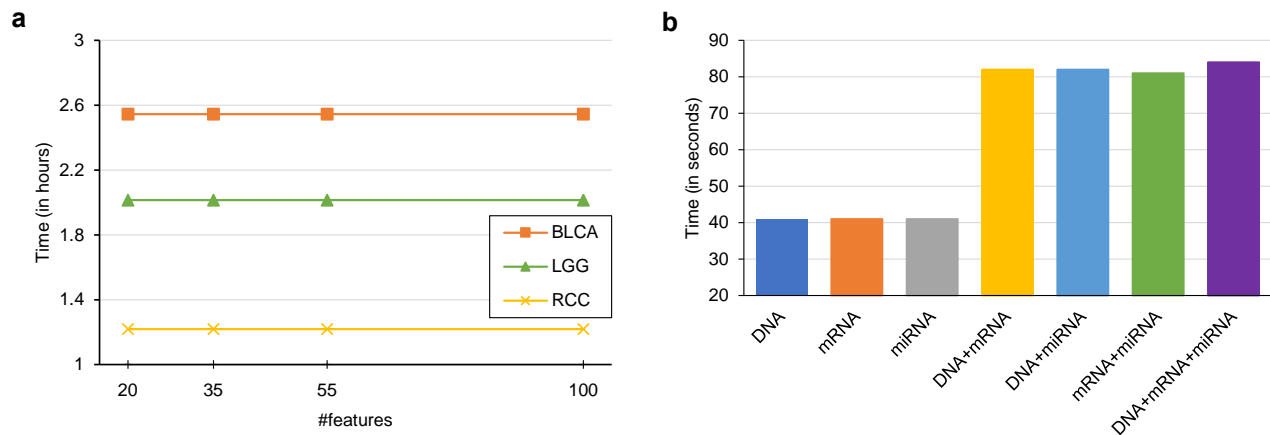


**Fig. S8. Execution time analysis of HeteroGATomics.** **a**, Performance of the HeteroGATomics<sub>MAS</sub> module in terms of execution time with varying selected feature sizes across three datasets. **b**, Performance of the HeteroGATomics<sub>GAT</sub> module in terms of execution time for different combinations of omic modalities on the LGG dataset. Averaged execution times from 10-fold cross-validation are presented.

## References

1. Theodoridis, S. & Koutroumbas, K. *Pattern Recognition* (Elsevier Science, 2008).
2. Guyon, I., Weston, J., Barnhill, S. & Vapnik, V. Gene selection for cancer classification using support vector machines. *Mach. Learn.* **46**, 389–422 (2002).
3. Peng, H., Long, F. & Ding, C. Feature selection based on mutual information criteria of max-dependency, max-relevance, and min-redundancy. *IEEE Trans. Pattern Anal. Mach. Intell.* **27**, 1226–1238 (2005).
4. El-Manzalawy, Y., Hsieh, T.-Y., Shivakumar, M., Kim, D. & Honavar, V. Min-redundancy and max-relevance multi-view feature selection for predicting ovarian cancer survival using multi-omics data. *BMC Med. Genom.* **11**, 19–31 (2018).
5. Tabakhi, S. & Lu, H. Multi-agent feature selection for integrative multi-omics analysis. In *Annual International Conference of the IEEE Engineering in Medicine and Biology Society*, 1638–1642 (IEEE, 2022).
6. Ho, T. K. Random decision forests. In *Proceedings of the International Conference on Document Analysis and Recognition*, vol. 1, 278–282 (IEEE, 1995).

7. Hoerl, A. E. & Kennard, R. W. Ridge regression: biased estimation for nonorthogonal problems. *Technometrics* **12**, 55–67 (1970).
8. Wang, T. *et al.* MOGONET integrates multi-omics data using graph convolutional networks allowing patient classification and biomarker identification. *Nat. Commun.* **12**, 3445 (2021).
9. Li, J.-H., Liu, S., Zhou, H., Qu, L.-H. & Yang, J.-H. starBase v2. 0: decoding miRNA-ceRNA, miRNA-ncRNA and protein–RNA interaction networks from large-scale CLIP-Seq data. *Nucleic Acids Res.* **42**, D92–D97 (2014).
10. Setiono, R. & Liu, H. Neural-network feature selector. *IEEE Trans. Neural Netw.* **8**, 654–662 (1997).
11. Amjad, R. A., Liu, K. & Geiger, B. C. Understanding neural networks and individual neuron importance via information-ordered cumulative ablation. *IEEE Trans. Neural Netw. Learn. Syst.* **33**, 7842–7852 (2022).
12. Szklarczyk, D. *et al.* The STRING database in 2023: protein–protein association networks and functional enrichment analyses for any sequenced genome of interest. *Nucleic Acids Res.* **51**, D638–D646 (2023).
13. Kamburov, A. & Herwig, R. ConsensusPathDB 2022: molecular interactions update as a resource for network biology. *Nucleic Acids Res.* **50**, D587–D595 (2022).
14. Sondka, Z. *et al.* COSMIC: a curated database of somatic variants and clinical data for cancer. *Nucleic Acids Res.* **52**, D1210–D1217 (2024).
15. Chakravarty, D. *et al.* OncoKB: a precision oncology knowledge base. *JCO Precis. Oncol.* **2017**, PO.17.00011 (2017).
16. Repana, D. *et al.* The Network of Cancer Genes (NCG): a comprehensive catalogue of known and candidate cancer genes from cancer sequencing screens. *Genome Biol.* **20**, 1–12 (2019).
17. Fey, M. & Lenssen, J. E. Fast graph representation learning with PyTorch Geometric. In *ICLR Workshop on Representation Learning on Graphs and Manifolds* (2019).
18. Paszke, A. *et al.* PyTorch: an imperative style, high-performance deep learning library. In *Advances in Neural Information Processing Systems*, vol. 32 (NeurIPS, 2019).
19. Pedregosa, F. *et al.* Scikit-learn: machine learning in Python. *J. Mach. Learn. Res.* **12**, 2825–2830 (2011).
20. Harris, C. R. *et al.* Array programming with NumPy. *Nature* **585**, 357–362 (2020).
21. The pandas development team. pandas-dev/pandas: Pandas 2.1.1. Zenodo <https://doi.org/10.5281/zenodo.8364959> (2023).
22. Virtanen, P. *et al.* SciPy 1.0: fundamental algorithms for scientific computing in Python. *Nat. Methods* **17**, 261–272 (2020).
23. Falcon, W. & The PyTorch Lightning team. PyTorch Lightning 2.1.3. Zenodo <https://doi.org/10.5281/zenodo.10419201> (2023).
24. Kingma, D. P. & Ba, J. Adam: a method for stochastic optimization. In *International Conference for Learning Representations (ICLR, 2015)*.
25. Li, J. *et al.* Feature selection: a data perspective. *ACM Comput. Surv.* **50**, 94 (2018).
26. Chen, T. & Guestrin, C. XGBoost: a scalable tree boosting system. In *Proceedings of the ACM SIGKDD International Conference on Knowledge Discovery and Data Mining*, 785–794 (ACM, 2016).
27. Dorigo, M. & Gambardella, L. M. Ant colony system: a cooperative learning approach to the traveling salesman problem. *IEEE Trans. Evol. Comput.* **1**, 53–66 (1997).
28. Dorigo, M. & Blum, C. Ant colony optimization theory: a survey. *Theor. Comput. Sci.* **344**, 243–278 (2005).
29. Dorigo, M., Di Caro, G. & Gambardella, L. M. Ant algorithms for discrete optimization. *Artif. life* **5**, 137–172 (1999).